

1 **Direct observation of time-dependent coherent chiral tunneling**
2 **dynamics.**

3 Wenhao Sun, Denis S. Tikhonov,^{*} and Melanie Schnell[†]

4 *Deutsches Elektronen-Synchrotron DESY,*
5 *Notkestr. 85, 22607 Hamburg, Germany*

6 (Dated: December 10, 2024)

arXiv:2412.06682v1 [quant-ph] 9 Dec 2024

Abstract

Superpositions of handed molecular states give rise to achiral eigenstates, delocalized across a double-well potential via tunneling. A coherent superposition of these energy eigenstates could dynamically relocalize the molecules into chiral states, which has only been addressed theoretically. Here, we present a microwave six-wave mixing pump-probe study to create and probe coherent chiral tunneling dynamics in a rotational state. Through a time-resolved scheme, we uncover the periodic time evolution of the induced chiral wavepacket under field-free conditions. Moreover, we demonstrate precise phase control of this coherence via phase modulation during pump excitation.

7 *Introduction.*—Molecular chirality is a fascinating phenomenon where a molecule can
8 exist in left- and right-handed forms that are mirror images of each other, also known as
9 enantiomers. Although enantiomers share nearly identical physical properties, their non-
10 superimposable structures often lead to distinct chemical and biological behaviors. Despite
11 its widespread presence in our everyday life, molecular chirality remains a field rich in
12 unresolved mysteries, such as its origin in physics and biological homochirality [1, 2]. In
13 quantum theory, chiral molecules are described as two localized chiral states in a double-
14 well system [3, 4], as depicted in FIG. 1. The two potential wells are nearly equivalent, with
15 a very small energy difference (ΔE_{PV}) due to the parity-violation effect [5]. Governed by the
16 double-well potential, molecules may exist in non-stationary chiral configurations localized in
17 one of the wells or in stationary achiral superposition eigenstates delocalized over both wells
18 in equal amounts [6, 7]. The latter appears as the result of ‘fast’ tunneling of chiral states
19 through the potential barrier, generating two eigenstates of symmetric and antisymmetric
20 parity ($|\pm\rangle$) with respect to spatial inversion [1, 3, 4]. Nevertheless, the boundary between
21 the classical-like chiral states and quantum-mechanical superposition states are still unclear,
22 which is commonly referred to as Hund’s paradox [4, 8].

23 Addressing such problems requires high-resolution spectroscopy and precise quantum
24 control of molecular systems using external fields. Based on the quantum superposition
25 principle, two stable enantiomers (R and S) can be prepared as a quantum superposition
26 with well-defined parity ($|\pm\rangle$) through subtle matter-wave interactions, generating an observ-

* Current address: Center for Free-Electron Laser Science CFEL, Deutsches Elektronen-Synchrotron DESY,
Notkestr. 85, 22607 Hamburg, Germany.

† melanie.schnell@desy.de; Institute of Physical Chemistry, Christian-Albrechts-Universität zu Kiel, Max-
Eyth-Str. 1, 24118 Kiel, Germany

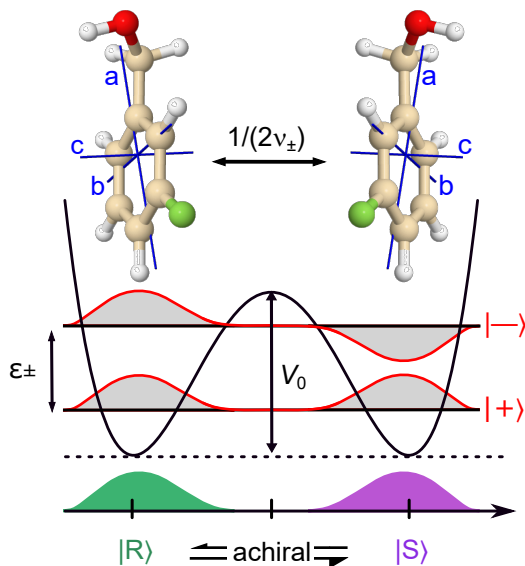


FIG. 1. Double-well potential of 3-fluorobenzyl alcohol. Molecular geometries of *R*- and *S*-3-fluorobenzyl alcohol are shown in their inertial principal axis systems (PAS). The $|R\rangle$ and $|S\rangle$ states represent the localized right- and left-handed chiral states, whereas the $|\pm\rangle$ states denote achiral energy eigenstates with opposite parity in the vibronic ground state. The energy difference $\varepsilon_{\pm} = h\nu_{\pm}$ between the $|\pm\rangle$ states in the $J_{K_a K_c} = 0_{00}$ state of 3-fluorobenzyl alcohol, expressed through the tunneling frequency ν_{\pm} , has been experimentally determined to be $\nu_{\pm} = 0.818(12)$ MHz [16]. Accordingly, the transfer time from one chiral form to the other form is $1/(2\nu_{\pm})$, that is 0.611 μ s.

27 able tunneling dynamics [9–11]. In turn, coherent superposition of the vibrational-tunneling
 28 $|\pm\rangle$ eigenstates will lead to coherent chiral tunneling within the double-well potential [12–
 29 14]. This gives rise to a non-stationary chiral wavepacket, periodically oscillating at the
 30 tunneling frequency under field-free conditions. However, it still remains a challenging task
 31 to experimentally establish the quantum conversion between chiral states and delocalized
 32 superposition eigenstates [15].

33 Over the past decade, the microwave three-wave mixing (M3WM) technique, a resonant,
 34 coherent, and non-linear approach, has demonstrated its robust capability in preparing co-
 35 herent states for stable chiral molecules with enantiomeric sensitivity [17–20]. This technique
 36 was later adapted to create a coherent superposition of energy eigenstates within the ro-

37 tational states of transiently chiral molecules [21]. In an earlier experiment using benzyl
38 alcohol as a model, an enantiomeric excess was induced from the quantum racemic mixture,
39 suggesting the successful preparation of the coherent tunneling state [21]. However, a direct
40 observation of its time-dependent dynamics was not achieved due to its rate being faster
41 than the capabilities of the experimental setup.

42 Herein, we demonstrated a pump-probe experiment using a quantum racemic mixture
43 of 3-fluorobenzyl alcohol, revealing the field-free time evolution of the non-stationary chiral
44 wavepacket arising from coherent tunneling. The experiment begins with a pump cycle
45 that prepares a coherent superposition of the $|\pm\rangle$ eigenstates in a chosen rotational level,
46 driven by a combination of two-photon and one-photon excitations. Although the resulting
47 dynamically localized chiral wavepacket is non-observable due to the forbidden nature of
48 the $|+\rangle \leftrightarrow |-\rangle$ transition, it produces a macroscopic enantiomeric excess, which can be
49 detected by a subsequent probe cycle. Two probing sub-cycles are simultaneously driven
50 to induce polarizations at two listen transitions. The observed time-domain listen signal
51 exhibits interference beats in the form of a free induction decay (FID). By varying the time
52 delay between the pump and probe cycles, we capture the time evolution of these beats
53 under field-free conditions, offering direct observation of the time-dependent coherent chiral
54 tunneling dynamics in the target state. Additionally, we demonstrate that phase modulation
55 during the pump excitation allows precise control over the phase of the induced coherent
56 tunneling.

57 *Theory.*—As can be seen in FIG. 1, the tunneling motion in 3-fluorobenzyl alcohol arises
58 from a concerted rotation of the CH_2OH and OH groups, transferring one enantiomer into the
59 other enantiomeric form. This large-amplitude motion (LAM) is hindered by a barrier of 1.9
60 kJ/mol, resulting in a tunneling frequency of $\nu_{\pm} = 0.818(12)$ MHz [16]. Thus, 3-fluorobenzyl
61 alcohol exists in the achiral superposition eigenstates, whereas the right- and left-handed
62 chiral states are non-stationary. Due to the selection rules, direct excitation between the
63 eigenstates of opposite parity ($|+\rangle \leftrightarrow |-\rangle$) is dipole-forbidden within the same rotational
64 level. But even if possible, a one-photon excitation cannot create a chiral ensemble, but
65 only a racemic mixture [22]. To create a macroscopic ensemble of coherently superposed $|\pm\rangle$
66 states, a microwave excitation scheme, adapted from the M3WM approach, is proposed, as
67 presented in FIG. 2a.

68 In the level diagram, each state is labeled with the rotational level $|J_{K_a K_c}\rangle$ and the

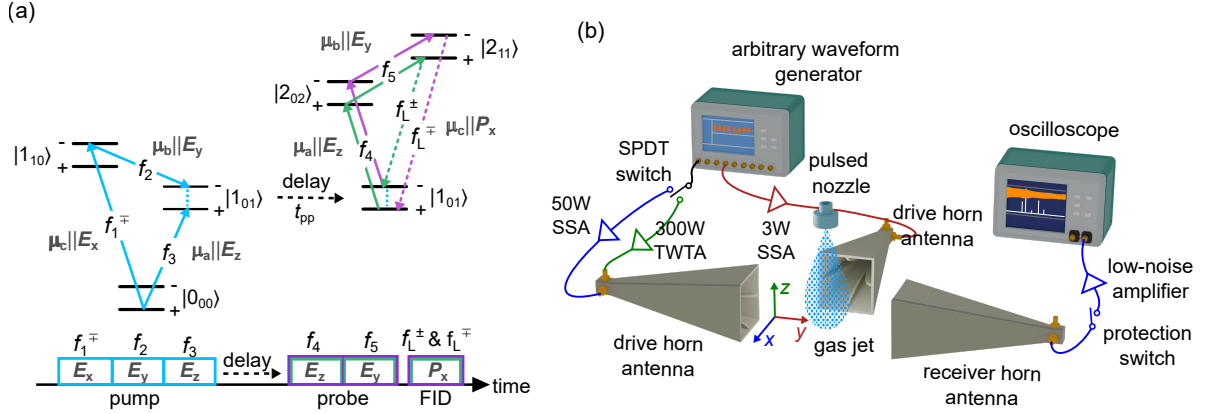


FIG. 2. Level scheme and experimental setup for the pump-probe measurement. (a). Pump-probe level diagram starting from the $|000^+\rangle$ rotational state, with the pulse sequence shown below. The energy levels are marked with the rotational state $|J_{K_a K_c}\rangle$ and the superposition parity \pm . The M -degeneracy of rotational levels is omitted for clarity. Intrastate transitions are denoted using f_i , where tunneling doublets can be excited using the same frequency, while the interstate transition components are labeled explicitly with f_i^\mp/f_i^\pm . For each transition, the corresponding dipole-moment component in the molecular frame and the polarization direction of the microwave field in the laboratory frame are indicated using $\mu_\alpha \parallel \mathbf{E}_\beta$ ($\alpha = a, b, c$; $\beta = x, y, z$). In both pump and probe cycles, excitations of the three types of transitions take place in mutually orthogonal polarization directions. (b). Schematic of the Fourier transform microwave spectrometer COMPACT used in this work. See Supplementary Section II B for detailed demonstration and abbreviations.

69 associated parity \pm , with J being the total angular momentum quantum number, and
70 K_a and K_c being projections of this momentum onto the a - and c - principal axes in the
71 molecular frame. As the tunneling motion inverts the electric dipole-moment component
72 along the c -principal axis, μ_c -type rotational transitions (f_1 and f_L) are allowed between
73 tunneling substates of opposite parity ($f_1^\mp: |+\rangle \rightarrow |-\rangle$ and $f_L^\pm: |-\rangle \rightarrow |+\rangle$), which are called
74 interstate transitions. The frequency difference of the two interstate transition components
75 is approximately $\Delta\nu = 2\varepsilon_\pm/h$, which is 1.64 MHz in this system. On the other hand, μ_a -
76 and μ_b -type transitions ($f_2 - f_5$) are only allowed for intrastate transitions ($|+\rangle \rightarrow |+\rangle$ and
77 $|-\rangle \rightarrow |-\rangle$). The splittings of intrastate transitions are small for 3-fluorobenzyl alcohol, so
78 each tunneling doublet can be simultaneously excited using the same frequency.

79 Starting from a μ_c -type transition f_1^\mp , molecules initially populating the $|0_{00}^+\rangle$ state
80 are excited to $|1_{01}^-\rangle$ and $|1_{01}^+\rangle$ states, following the two-photon ($|0_{00}^+\rangle \xrightarrow{f_1^\mp} |1_{10}^-\rangle \xrightarrow{f_2}$
81 $|1_{01}^-\rangle$) and one-photon ($|0_{00}^+\rangle \xrightarrow{f_3} |1_{01}^+\rangle$) pathways (FIG. 2a), respectively. The two-path
82 excitation creates a coherent superposition of the $|\pm\rangle$ eigenstates in the $|1_{01}\rangle$ rotational level,
83 even though one-photon excitation is strictly forbidden. Disregarding the absolute phase of
84 this superposition, the initial state of the induced coherence in $|1_{01}\rangle$ can be described as

$$\Psi(t=0) = \frac{1}{\sqrt{2}} (|1_{01}^+\rangle + \exp(i\phi)|1_{01}^-\rangle), \quad (1)$$

85 where $|1_{01}^\pm\rangle = \frac{1}{\sqrt{2}}(|R_{101}\rangle \pm |S_{101}\rangle)$ with $|R_{101}\rangle$ and $|S_{101}\rangle$ being the non-stationary wavefunc-
86 tions of R and S enantiomer in the $|1_{01}\rangle$ state and ϕ is the pulse-controlled initial phase
87 of the wavepacket. This initial state corresponds to a chiral wavepacket localized in one of
88 the potential wells, which subsequently undergoes field-free time evolution governed by the
89 LAM tunneling motion. Again, as the $|1_{01}^-\rangle \leftrightarrow |1_{01}^+\rangle$ transition is dipole-forbidden, this
90 tunneling coherence cannot be spectroscopically probed.

91 Instead, the chiral wavepacket produces a macroscopic enantiomeric excess (ee) in the
92 $|1_{01}\rangle$ state [21]. The resulting ee follows the same time-dependent dynamics as the non-
93 stationary chiral wavepacket,

$$\langle\psi(t)|\hat{e}e_{1_{01}}|\psi(t)\rangle \propto \overbrace{-\sin(\Omega_1\tau_1) \sin\left(\frac{\Omega_2\tau_2}{2}\right) \sin\left(\frac{\Omega_3\tau_3}{2}\right)}^{\propto|ee|} \cdot \sin(2\pi\nu_\pm t + \varphi_1 - \varphi_2 - \varphi_3 + \Phi), \quad (2)$$

94 where the $\hat{e}e$ operator for the $|1_{01}\rangle$ state can be expressed as [21]

$$\hat{e}e_{1_{01}} = |R_{101}\rangle\langle R_{101}| - |S_{101}\rangle\langle S_{101}| = |1_{01}^+\rangle\langle 1_{01}^-| + |1_{01}^-\rangle\langle 1_{01}^+|, \quad (3)$$

95 Ω_k , τ_k and φ_k denote the Rabi frequency, duration, and starting phase of the k -th microwave
96 pulse in the scheme, Φ represents the accumulated phase throughout the excitation process,
97 ν_\pm is the tunneling frequency in the $|1_{01}\rangle$ state, and t is the time.

98 As described in Equation 2, this ee observable oscillates at the tunneling frequency (ν_\pm)
99 under field-free conditions, with a constant amplitude proportional to $|ee|$. The time evo-
100 lution of ee can thus be monitored through a chiral-sensitive probe cycle, in which two
101 microwave excitations (f_4 and f_5) and an indirectly induced listen transition (f_L^\pm or f_L^\mp),
102 combined with the tunneling coherence, create a closed loop. In particular, as f_4 and f_5 are
103 associated with intrastate transitions, two probing sub-cycles can be simultaneously driven,

104 sensing the same tunneling coherence from opposite directions. At the two μ_c -type interstate
105 listen transitions, the signal phases should be linearly dependent on the tunneling coherence
106 oscillation ($2\pi\nu_{\pm}t$), while the amplitudes are proportional to $|ee|$. The detailed theoretical
107 derivations are provided in the Supplementary Section I B.

108 *Experiment*—The experiments are performed with an adapted broadband chirped-pulse
109 FTMW spectrometer, as shown in FIG. 2b. The principles and the modifications of the
110 spectrometer have been described in detail elsewhere [21, 23]. A brief description is provided
111 here. The spectrometer is equipped with a two-channel arbitrary waveform generator (AWG)
112 with a maximum sampling rate of 24 GSa/s, which is capable of generating microwave pulses
113 below 6 GHz in a two-channel mode. Microwave pulses produced from the same AWG
114 channel can be further divided by a single-pole double-throw (SPDT) PIN diode switch
115 with nanosecond switching capability. In this way, microwave pulses can be separately
116 fed into dedicated amplifiers for power amplification and broadcast into the spectrometer
117 chamber in designated polarization directions ($\mathbf{E}_x, \mathbf{E}_y, \mathbf{E}_z$). The latter is achieved through
118 two dual-polarization horn antennae oriented perpendicularly to each other.

119 In this study, 3-fluorobenzyl alcohol is employed as the molecular model. The sample
120 is commercially available from Fisher Scientific with a chemical purity of 98 % and used
121 without further purification. The liquid sample is held in a home-built heatable reservoir,
122 which is integrated into the solenoid nozzle valve (General Valve Series 9) and maintained
123 at 100 °C. The diameter of the orifice is 1 mm. The sample vapor is diluted into neon carrier
124 gas at a backing pressure of 3 bar and supersonically expanded into the vacuum chamber
125 perpendicular to the propagation directions of the microwave radiation. The background
126 pressure in the vacuum chamber is approximately 10^{-6} mbar, and the solenoid valve is
127 operated at 8 Hz. Molecules in the jet expansion are cooled down to a rotational temperature
128 (T_{rot}) of about 1 K. In the interaction region, the transmitted microwave pulse sequence
129 consecutively polarizes these molecules eight times. Following each interaction sequence,
130 the decay of the macroscopic polarization of the molecular ensemble is collected by a dual-
131 polarization receiver horn facing one of the drive horns. The free induction decay (FID)
132 signals are recorded with a duration of 40 μs and averaged on a fast digital oscilloscope,
133 which is used for further data processing. This provides sufficient time resolution to unveil
134 the tunneling dynamics of 3-fluorobenzyl alcohol.

135 *Results*.—Prior to the pump-probe experiments, the excitation microwave pulses are in-

136 individually optimized by measuring Rabi cycles as a function of pulse duration. More details
 137 can be found in Supplementary Section II C. In general, a Rabi $\pi/2$ pulse can evenly dis-
 138 tribute the population in a two-level system, achieving maximum coherence between the
 139 states. In contrast, a π pulse inverts the population between the two levels, which can be
 140 applied to transfer prepared coherence in a three-level system [24]. Ideally, f_1^\mp and f_4 should
 141 be $\pi/2$ pulses, whereas f_2 , f_3 , and f_5 should be π pulses. However, in this scheme, f_1^\mp and
 142 f_3 are optimized to near $\pi/2$ conditions, to minimize the off-resonance excitation of the f_1^\pm
 143 transition and the population inversion between the $|1_{01}^- \rangle$ and $|0_{00}^- \rangle$ states, respectively.
 144 The applied pulse conditions are summarized in Supplementary Table S2.

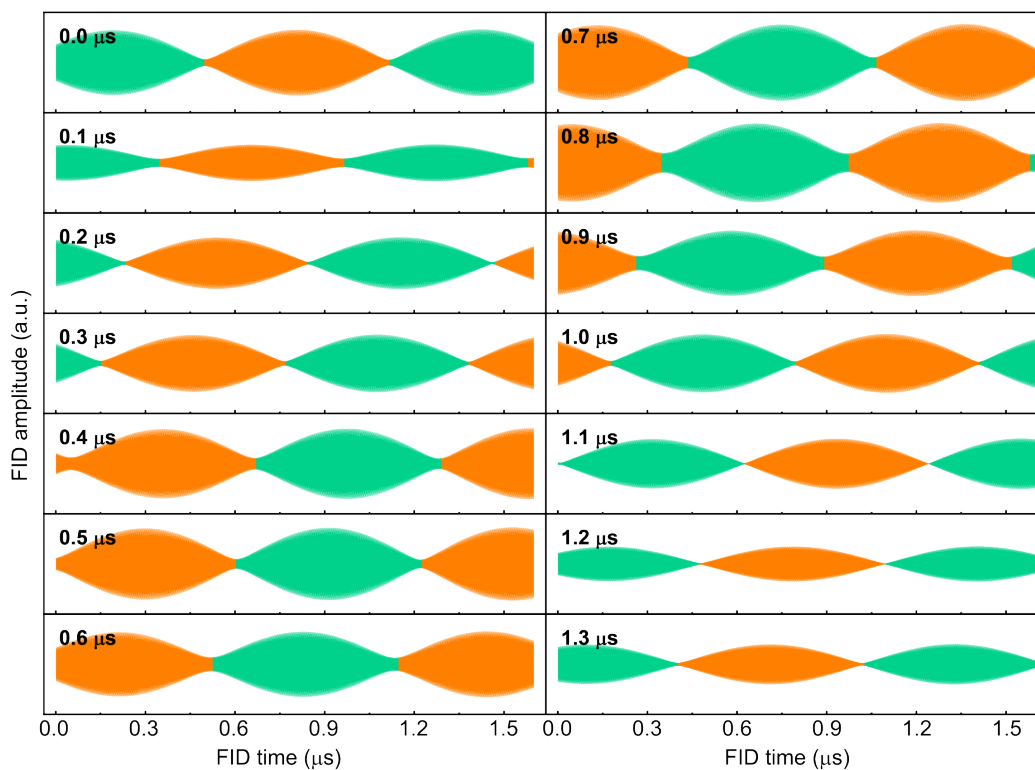


FIG. 3. Time evolution of the beating listen signals. The first $1.6 \mu\text{s}$ of the filtered experimental FID signals are shown at different pump-probe delays, with the delay time (t_{pp}) indicated in the upper left corner. The y axis ranges from -4 to 4 nV. The original data are filtered at the listen frequencies (f_L^\pm : 6385.55 MHz and f_L^\mp : 6387.18 MHz) using a bandpass Butterworth filter (6th-order) with a bandwidth of 60 kHz. The neighboring beats are highlighted in orange and green to indicate the sign change of the cosine-shaped beat envelopes.

145 Accordingly, the microwave pulse sequence is constructed for the pump-probe experi-
 146 ments, as shown in FIG. 2a. As the tunneling period of 3-fluorobenzyl alcohol in state $|1_{01}\rangle$
 147 is approximately $1.2 \mu\text{s}$, the entire probe cycle is shifted in our experiments by $0\text{--}1.3 \mu\text{s}$ in
 148 $0.1 \mu\text{s}$ steps relative to the pump cycle, while the durations and phases of all microwave
 149 pulses remain fixed. FIG. 3 displays the first $1.6 \mu\text{s}$ of the time-domain FID signals recorded
 150 at each delay time (t_{pp}). Owing to the similar frequencies of f_L^\pm and f_L^\mp , the FID traces
 151 exhibit clear interference beats, with a carrier-wave frequency of $(f_L^\pm + f_L^\mp)/2$ and a beat
 152 frequency of $(f_L^\pm - f_L^\mp)/2$. Note that a full cycle of the interference includes two beats,
 153 which are masked in two colors for the sake of clarity. As the delay time varies, the beating
 154 signals exhibit clear shifts, highlighting the non-stationary nature of the localized wavepacket
 155 in the $|1_{01}\rangle$ rotational level. This periodic time evolution shows good consistency with the
 156 tunneling period of 3-fluorobenzyl alcohol.

157 After applying a fast Fourier transformation, the obtained intensities and phases at the

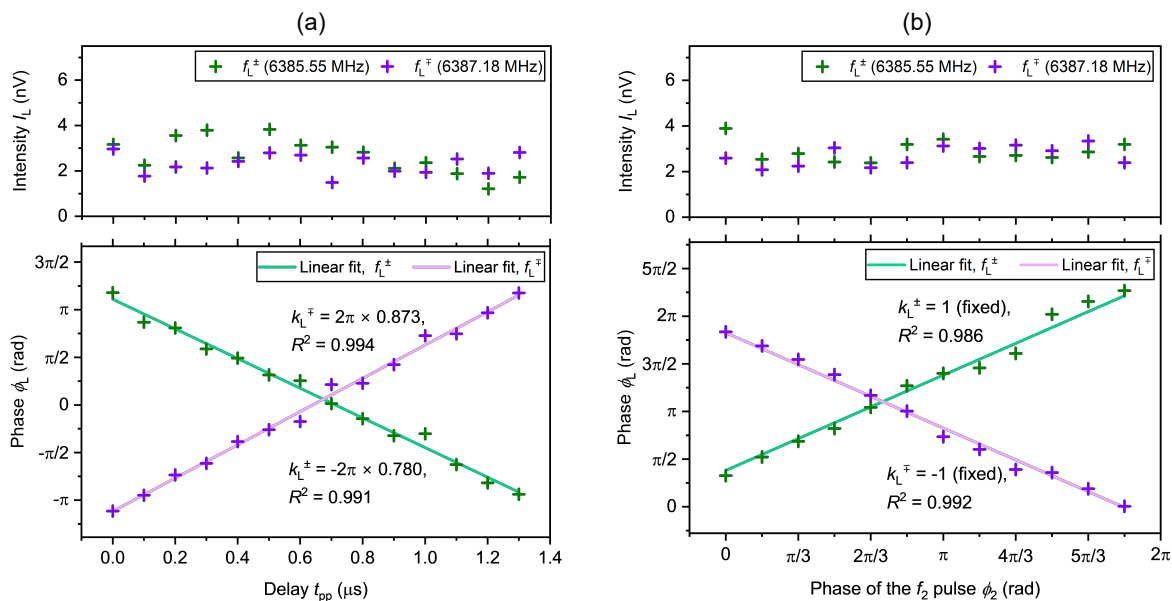


FIG. 4. Results of the microwave pump-probe experiments. Panels A and B show the intensities (I_L) and phases (ϕ_L) at the listen transitions, f_L^\pm (6385.55 MHz) and f_L^\mp (6387.18 MHz), as a function of time delay (t_{pp} , in μs) and phase of the f_2 pulse (ϕ_2 , in radians), respectively. The scatter points display the experimental results. Each point is averaged from 5×10^5 FID acquisitions, which takes about 2.2 h. The colored lines represent the linear fits on the phase results of f_L^\pm and f_L^\mp , with the slopes (k_L) and R-squared values (R^2) provided.

158 listen transitions are presented in FIG. 4a. Considering the signal fluctuation over the
 159 long measurement time and the interference from a counterpart pump cycle starting from
 160 $|0_{00}^-\rangle$, the observed intensities indicate that the amplitudes of the listen transitions are
 161 relatively stable. The corresponding phases exhibit linear correlations with the delay time
 162 — negative for f_L^\pm and positive for f_L^\mp , as the two sub-cycles probe the tunneling coherence
 163 from opposite directions. Both the intensity and phase behaviors are consistent with the
 164 theoretical model.

165 Linear least-squares fits are performed on the phase results of f_L^\pm and f_L^\mp , respectively
 166 (FIG. 4a). For both fits, the R-squared values (R^2) are higher than 0.99, suggesting nearly
 167 perfect linear correlations between the phase evolution and the time delay. The absolute
 168 values of the slopes, $|k_L^\pm|$ and $|k_L^\mp|$, represent the tunneling frequency in radians ($2\pi\nu_\pm$)
 169 detected by each probing sub-cycle. The two fitted tunneling frequencies deviate almost
 170 symmetrically from the spectroscopically determined value ($2\pi \times 0.82$ MHz) by approxi-
 171 mately 5%. This deviation can be attributed to the perturbation of the other cycle starting
 172 from the $|0_{00}^-\rangle$ state, similar to what was observed in Ref. 25. A detailed demonstration is
 173 provided in the Supplementary Section II D. By averaging these two slopes, the tunneling
 174 frequency from this time-resolved pump-probe experiment is estimated to be 0.827(15) MHz,
 175 precisely matching the spectroscopically determined values of 0.82 MHz, which falls in the
 176 frequency accuracy (10 kHz) of our spectrometer.

177 Furthermore, the phase of the coherent superposition of the $|\pm\rangle$ eigenstates can be finely
 178 modulated using the phases of the three pump pulses (φ_1 , φ_2 and φ_3). This allows for precise
 179 control over the positioning of the induced chiral wavepacket ($\Psi(t)$) within the double-well
 180 potential. To examine this, a phase-controlled pump-probe experiment is conducted, where
 181 the phase of the f_2 pulse (φ_2) is scanned from 0 to 2π in steps of $\pi/6$ radians, without ap-
 182 plying a delay time between the pump and probe cycles. According to Equation 2, constant
 183 amplitudes and linear φ_2 -phase dependence are expected for the listen transitions (f_L^\pm and
 184 f_L^\mp), similar to the time-resolved pump-probe experiment (FIG. 4a). The experimental
 185 results are provided in FIG. 4b, in convincing agreement with the expectations. The phases
 186 are linearly fitted with the slope constrained to ± 1 . The R^2 values, close to 0.99, confirm the
 187 linear phase-phase correlation. As the φ_2 and $2\pi\nu_\pm t$ terms in Equation 2 have opposite signs,
 188 the observed phase-phase and phase-delay correlations exhibit opposite trends for the same
 189 listen transition. By utilizing phase control, the chiral wavepacket can be readily prepared

190 at various coherence phases for further advanced experiments, such as enantiomer-selective
191 excitation, without the need to adjust experimental timing.

192 *Discussion.*—Time-dependent coherent tunneling dynamics had, until now, solely been
193 addressed theoretically. Our proof-of-concept experiment offers direct evidence to the theory
194 model, exemplifying wave-particle duality and the superposition principle at the molecular
195 level. Compared to the previously studied benzyl alcohol, which has a tunneling frequency
196 of about 493 MHz [21], the relatively slow tunneling motion in 3-fluorobenzyl alcohol with
197 frequency of 0.8 MHz offers two key advantages. First, it enables the simultaneous excitation
198 of two probing sub-cycles, producing a listen signal in the form of frequency beats. Second,
199 the sub-MHz tunneling motion is well-suited to the present sampling rate and duration of
200 the FID. Therefore, the evolution of the beating signal is clearly observed on a microsecond
201 timescale in the time domain. Each beat in FIG. 3 can be considered an M3WM signal from
202 a localized state of a given chirality; thus, the observed oscillating signal originates from the
203 field-free time-dependent coherent chiral tunneling dynamics in the target rotational state.

204 It is important to note that the coherent superposition of the $|\pm\rangle$ eigenstates, driven
205 by the pump cycle, can be applied universally to all tunneling molecules, regardless of the
206 tunneling frequency and the coherence readout scheme. For fast-tunneling chiral molecules
207 like benzyl alcohol, the increased frequency differences between tunneling components lead to
208 better separation of sub-cycles in the scheme, reducing the interference between them and
209 thus improving the efficiency of coherent state preparation. However, it also complicates
210 the observation of coherent tunneling dynamics through time-domain frequency beats, as
211 simultaneous excitation of both probing sub-cycles becomes impractical. Alternatively, the
212 linear phase-delay dependence can be generally applied to monitor these dynamics, as shown
213 in FIG. 4a.

214 This study, which uncovers tunneling dynamics in a pure rotational state within the
215 ground vibronic state, serves as a streamlined analogue to previous computational investi-
216 gations of pure vibrational and rotational-vibrational model systems [1, 12, 26]. Our results
217 lay the groundwork for future experimental exploration involving both vibrational and rota-
218 tional degrees of freedom with coherent laser fields. By employing tailored microwave fields,
219 this coherent approach can be further extended to control the tunneling dynamics, achieving
220 coherent inhibition and enhancement of tunneling. Through the coherent inhibition strategy,
221 similar with coherent destruction of tunneling in laser physics [14], the induced dynamically

222 localized chiral wavepacket can be selectively confined within one of the potential wells,
223 enabling a complete transition from delocalized $|\pm\rangle$ eigenstates to localized chiral states
224 $|R\rangle$ or $|S\rangle$. This may open the door to resolving Hund’s paradox [3, 4]. The controllable,
225 time-dependent quantum dynamics also finds its application in examining chiral molecular
226 systems for perturbation effects from parity violation, exploring the symmetry of space and
227 time and its violation in chiral molecules, particularly in cases where ΔE_{PV} is expected to
228 be significantly larger than ΔE_{\pm} [27–29].

229 *Acknowledgments.*—This work has been funded by the Deutsche Forschungsgemeinschaft
230 (DFG, German Research Foundation) - Projektnummer 328961117 - SFB 1319 ELCH.

231 *Author contributions statement.*—All authors conceived the experiment, W.S. conducted
232 the experiments, and W.S. and D.T. analyzed the results. All authors reviewed the
233 manuscript.

234 *Data availability.*—All the data supporting this study’s findings are available within the
235 main text and the Supplementary Material and from the corresponding author on request.

236 *Competing interests.*—The authors declare no competing interests.

-
- 237 [1] M. Quack, Structure and dynamics of chiral molecules, *Angew. Chem. Int. Ed.* **28**, 571 (1989).
238 [2] N. Fujii and T. Saito, Homochirality and life, *Chem. Rec.* **4**, 267 (2004).
239 [3] F. Hund, Zur Deutung der Molekelspektren. i, *Zeitschrift für Physik* **40**, 742 (1927).
240 [4] F. Hund, Zur Deutung der Molekelspektren. iii. Bemerkungen über das Schwingungs-und
241 Rotations-spektrum bei Molekeln mit mehr als zwei Kernen, *Zeitschrift für Physik* **43**, 805
242 (1927).
243 [5] M. Quack, How important is parity violation for molecular and biomolecular chirality?, *Angew.*
244 *Chem. Int. Ed.* **41**, 4618 (2002).
245 [6] S. Mason, Biomolecular homochirality, *Chem. Soc. Rev.* **17**, 347 (1988).
246 [7] B. Fehrensens, D. Luckhaus, and M. Quack, Stereomutation dynamics in hydrogen peroxide,
247 *Chem. Phys.* **338**, 90 (2007).
248 [8] H. Primas, *Chemistry, quantum mechanics and reductionism: Perspectives in theoretical chem-*
249 *istry*, Vol. 24 (Springer Science & Business Media, 2013).
250 [9] J. A. Cina and R. A. Harris, On the preparation and measurement of superpositions of chiral

- 251 amplitudes, *J. Chem. Phys.* **100**, 2531 (1994).
- 252 [10] J. A. Cina and R. A. Harris, Superpositions of handed wave functions, *Science* **267**, 832 (1995).
- 253 [11] B. A. Stickler, M. Diekmann, R. Berger, and D. Wang, Enantiomer superpositions from
254 matter-wave interference of chiral molecules, *Phys. Rev. X* **11**, 031056 (2021).
- 255 [12] C. Fábri, R. Marquardt, A. G. Császár, and M. Quack, Controlling tunneling in ammonia
256 isotopomers, *J. Chem. Phys.* **150**, 10.1063/1.5063470 (2019).
- 257 [13] F. Bouakline, Does nuclear permutation symmetry allow dynamical localization in symmetric
258 double-well achiral molecules?, *J. Chem. Phys.* **152**, 10.1063/1.5141746 (2020).
- 259 [14] F. Grossmann, T. Dittrich, P. Jung, and P. Hänggi, Coherent destruction of tunneling, *Phys.*
260 *Rev. Lett.* **67**, 516 (1991).
- 261 [15] D. Brinks, F. D. Stefani, F. Kulzer, R. Hildner, T. H. Taminiou, Y. Avlasevich, K. Müllen,
262 and N. F. Van Hulst, Visualizing and controlling vibrational wave packets of single molecules,
263 *Nature* **465**, 905 (2010).
- 264 [16] S. Tang, Z. Xia, A. Maris, and W. Caminati, Tunnelling splittings in the rotational spectrum
265 of 3-fluoro-benzylalcohol, *Chem. Phys. Lett.* **498**, 52 (2010).
- 266 [17] E. Hirota, Triple resonance for a three-level system of a chiral molecule, *Proc. Jpn. Acad.*,
267 *Ser. B* **88**, 120 (2012).
- 268 [18] D. Patterson, M. Schnell, and J. M. Doyle, Enantiomer-specific detection of chiral molecules
269 via microwave spectroscopy, *Nature* **497**, 475 (2013).
- 270 [19] S. Eibenberger, J. Doyle, and D. Patterson, Enantiomer-specific state transfer of chiral
271 molecules, *Phys. Rev. Lett.* **118**, 123002 (2017).
- 272 [20] C. Pérez, A. L. Steber, A. Krin, and M. Schnell, State-specific enrichment of chiral conformers
273 with microwave spectroscopy, *J. Phys. Chem. Lett.* **9**, 4539 (2018).
- 274 [21] W. Sun, D. S. Tikhonov, H. Singh, A. L. Steber, C. Pérez, and M. Schnell, Inducing transient
275 enantiomeric excess in a molecular quantum racemic mixture with microwave fields, *Nat.*
276 *Commun.* **14**, 934 (2023).
- 277 [22] D. S. Tikhonov, A. Blech, M. Leibscher, L. Greenman, M. Schnell, and C. P. Koch, Pump-
278 probe spectroscopy of chiral vibrational dynamics, *Sci. Adv.* **8**, eade0311 (2022).
- 279 [23] D. Schmitz, V. Alvin Shubert, T. Betz, and M. Schnell, Multi-resonance effects within a
280 single chirp in broadband rotational spectroscopy: the rapid adiabatic passage regime for
281 benzonitrile, *J. Mol. Spectrosc.* **280**, 77 (2012).

- 282 [24] S. Lobsiger, C. Pérez, L. Evangelisti, K. K. Lehmann, and B. H. Pate, Molecular structure
283 and chirality detection by fourier transform microwave spectroscopy, *J. Phys. Chem. Lett.* **6**,
284 196 (2015).
- 285 [25] H. Singh, F. E. Berggötz, W. Sun, and M. Schnell, Chiral control of gas-phase molecules using
286 microwave pulses, *Angew. Chem. Int. Ed.* **62**, e202219045 (2023).
- 287 [26] S. Hervé, F. Le Quéré, and R. Marquardt, Generation of semiclassical and delocalized vibra-
288 tional wave packet motion of hf molecules oriented in an external static electric field, *J. Chem.*
289 *Phys.* **116**, 3300 (2002).
- 290 [27] M. Quack, Molecular quantum dynamics from high resolution spectroscopy and laser chem-
291 istry, *J. Mol. Struct.* **292**, 171 (1993).
- 292 [28] T. Li and A. Nadin, Correlation between time reversal symmetry and chirality in certain
293 molecular processes, *Chirality* **10**, 289 (1998).
- 294 [29] M. Quack and G. Seyfang, Tunnelling and Parity Violation in Chiral and Achiral Molecules:
295 Theory and High-resolution Spectroscopy, in *Tunnelling in Molecules: Nuclear Quantum Ef-*
296 *fects from Bio to Physical Chemistry* (The Royal Society of Chemistry, 2020).

Supplementary Material:
**Direct observation of time-dependent coherent chiral tunneling
dynamics.**

Wenhao Sun, Denis S. Tikhonov,^{*} and Melanie Schnell[†]

*Deutsches Elektronen-Synchrotron DESY,
Notkestr. 85, 22607 Hamburg, Germany*

(Dated: December 10, 2024)

^{*} Current address: Center for Free-Electron Laser Science CFEL, Deutsches Elektronen-Synchrotron DESY, Notkestr. 85, 22607 Hamburg, Germany.

[†] melanie.schnell@desy.de; Institute of Physical Chemistry, Christian-Albrechts-Universität zu Kiel, Max-Eyth-Str. 1, 24118 Kiel, Germany

Contents

I. Supplementary theoretical details	S1
A. Prerequisite information	S1
1. Two-level system	S1
2. Tunneling splitting system	S2
B. Derivation of the microwave pump-probe scheme	S3
1. Notations and assumptions	S3
2. Wavefunction evolution	S6
3. Induced enantiomeric excess after the pump cycle	S7
4. Listen signal in the pump-probe scheme	S9
II. Supplementary experimental details	S12
A. Experimental microwave pump-probe scheme	S12
B. Sample preparation and experimental setup	S14
C. Preparation of microwave fields	S16
D. Time-resolved pump-probe experiments.	S19
E. Phase-controlled pump-probe experiments.	S25
References	S26

I. Supplementary theoretical details

A. Prerequisite information

1. Two-level system

In order to theoretically describe the microwave pump-probe scheme, we will rely on the results and theoretical framework of the microwave six-wave mixing scheme (M6WM), as introduced in Ref. 1. Here, we will only provide the basics of the theoretical treatment. As the building block for the derivation, we will use the two-level system coupled to an external electromagnetic field through the dipole moment in a rotating-wave approximation (RWA), shown schematically in FIG. S1. The Hamiltonian can be written as

$$\hat{H} = \hat{H}_0 + \overbrace{\boldsymbol{\mu}_{mn} \mathbf{E}_0 \cdot \cos(\omega_{mn}t + \varphi) \cdot (|m\rangle\langle n| + |n\rangle\langle m|)}^{\hat{W}}, \quad (1)$$

where \hat{H}_0 is the Hamiltonian of the unperturbed molecular system with the eigenstates $|k\rangle$ and eigenenergies $\hbar\omega_k$ given by the stationary Schrödinger equation $\hat{H}_0|k\rangle = \hbar\omega_k|k\rangle$; \hat{W} is the interaction Hamiltonian, composed of the transition dipole moment $\boldsymbol{\mu}_{mn}$, the electric field linear polarization vector \mathbf{E}_0 , the angular frequency of the transition $\omega_{mn} = \omega_n - \omega_m$ from state $|m\rangle$ to state $|n\rangle$, and the carrier-envelope phase φ of the pulse. We assume that the system is initially present solely in state $|m\rangle$, while state $|n\rangle$ is unpopulated. In this

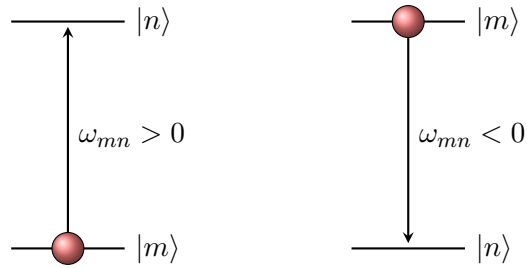


FIG. S1. A two-level system coupled with a resonant electric field with a frequency equal to the transition energy between states $|m\rangle$ and $|n\rangle$. The left system shows the transition from the lower energy state to the higher energy state, and the transition frequency of the absorption $\omega_{mn} > 0$ ($s_{mn} = +1$). The right figure shows the transition from the higher energy state to the lower energy state and the transition frequency of the emission $\omega_{mn} < 0$ ($s_{mn} = -1$).

case, the initial state of the system is

$$|\psi_0\rangle = c_m^{(0)}|m\rangle + c_n^{(0)}|n\rangle + \sum_{k \neq m, n} c_k^{(0)}|k\rangle, \quad (2)$$

where $c_i^{(0)}$ are the initial coefficients of the wavefunction ($c_n^{(0)} = 0$). After applying an excitation for time τ , and then switching the electric field off ($|E_0| = 0$) and monitoring the free evolution of the system, the wavefunction looks like

$$\begin{aligned} |\psi(t)\rangle = & \exp(-i\omega_m\tau - i\omega_mt) \cos\left(\frac{\Omega_{mn}\tau}{2}\right) c_m^{(0)}|m\rangle - \\ & - i \exp(-is_{mn}\varphi - i\omega_n\tau - i\omega_nt) \sin\left(\frac{\Omega_{mn}\tau}{2}\right) c_m^{(0)}|n\rangle + \\ & + \sum_{k \neq m, n} \exp(-i\omega_k\tau - i\omega_kt) c_k^{(0)}|k\rangle, \quad (3) \end{aligned}$$

where

$$\Omega_{mn} = \frac{\boldsymbol{\mu}_{mn} \cdot \mathbf{E}_0}{\hbar} \quad (4)$$

is the Rabi frequency of the transition $|m\rangle \rightarrow |n\rangle$, and s_{mn} is the sign of the transition frequency $\omega_{mn} \neq 0$ defined as (see FIG. S1)

$$s_{mn} = \text{sgn}(\omega_{mn}) = \begin{cases} +1 & \text{if } \omega_{mn} > 0, \\ -1 & \text{if } \omega_{mn} < 0. \end{cases} \quad (5)$$

In other words, if the transition is from the lower energy state to the higher energy one ($\omega_{mn} > 0$), then $s_{mn} = +1$ (absorption), and if the transition transfers population from the higher energy state to the lower one ($\omega_{mn} < 0$), then $s_{mn} = -1$ (emission).

2. Tunneling splitting system

In terms of tunneling splitting, we will have a pair of initial and final states $|m\pm\rangle$ and $|n\pm\rangle$, where $+$ and $-$ denote the state's parity levels (see FIG. S2), separated by a tunneling splitting energy $\hbar\Delta$. For intrastate transitions, the tunneling dynamics preserves the sign of the associated dipole-moment component, allowing transitions between states of the same parity ($|m\pm\rangle \rightarrow |n\pm\rangle$). However, for interstate transitions, as the sign of the dipole-moment component is inverted, the permitted transitions are between states of opposite parity (i.e., $|m\pm\rangle \rightarrow |n\mp\rangle$). This gives rise to an absorption/emission frequency doublet, separated by $2\Delta_{mn} = \Delta_m + \Delta_n$, as shown in FIG. S2.

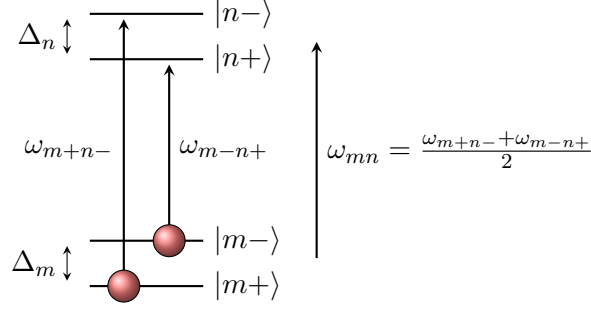


FIG. S2. Tunneling-split interstate system coupled with a symmetrically detuned electric field. Here, we show only the transitions from the lower energy state to the higher energy state ($s_{mn} = +1$).

To simultaneously address an interstate doublet with frequencies $\omega_{m+n-} = \omega_{n-} - \omega_{m+}$ and $\omega_{m-n+} = \omega_{n+} - \omega_{m-}$, a symmetrically detuned pulse can be applied with the center frequency $\omega_{mn} = \frac{\omega_{m+n-} + \omega_{m-n+}}{2}$, which is equally distant from the two transition frequencies in the frequency domain, since $\omega_{m+n-} = \omega_{mn} + \Delta_{mn}$ and $\omega_{m-n+} = \omega_{mn} - \Delta_{mn}$. In this case, both Rabi cycles will be increased in frequency to $\Omega = \sqrt{\Omega_0^2 + \Delta_{mn}^2}$, where Ω_0 (Equation 4) is the Rabi frequency of both interstate transitions (as their transition dipoles are identical), and also the magnitude of the Rabi oscillation will decrease by a factor of Ω_0/Ω [2]. In this symmetrically detuned case, it can be assumed that both transitions have approximately identical Rabi frequencies and excitation efficiencies. Moreover, when the excitation pulse is resonant with one of the transitions, the other transition is detuned by $2\Delta_{mn}$. Consequently, they oscillate at different Rabi frequencies, which are Ω_0 and $\sqrt{\Omega_0^2 + (2\Delta_{mn})^2}$. This allows us to drive the two transitions differently, even though they have close-by frequencies that cannot be separately driven due to the bandwidth of the microwave pulses.

B. Derivation of the microwave pump-probe scheme

1. Notations and assumptions

We will derive the evolution of the wavefunction in the microwave pump-probe experiment starting from states $|0+\rangle$ and $|0-\rangle$ (see FIG. S3). The first scheme connecting states $|0+\rangle$, $|1-\rangle$, $|2\pm\rangle$, $|3\pm\rangle$, and $|4\pm\rangle$ will be denoted hereinafter as (+)-cycle, while the second cycle,

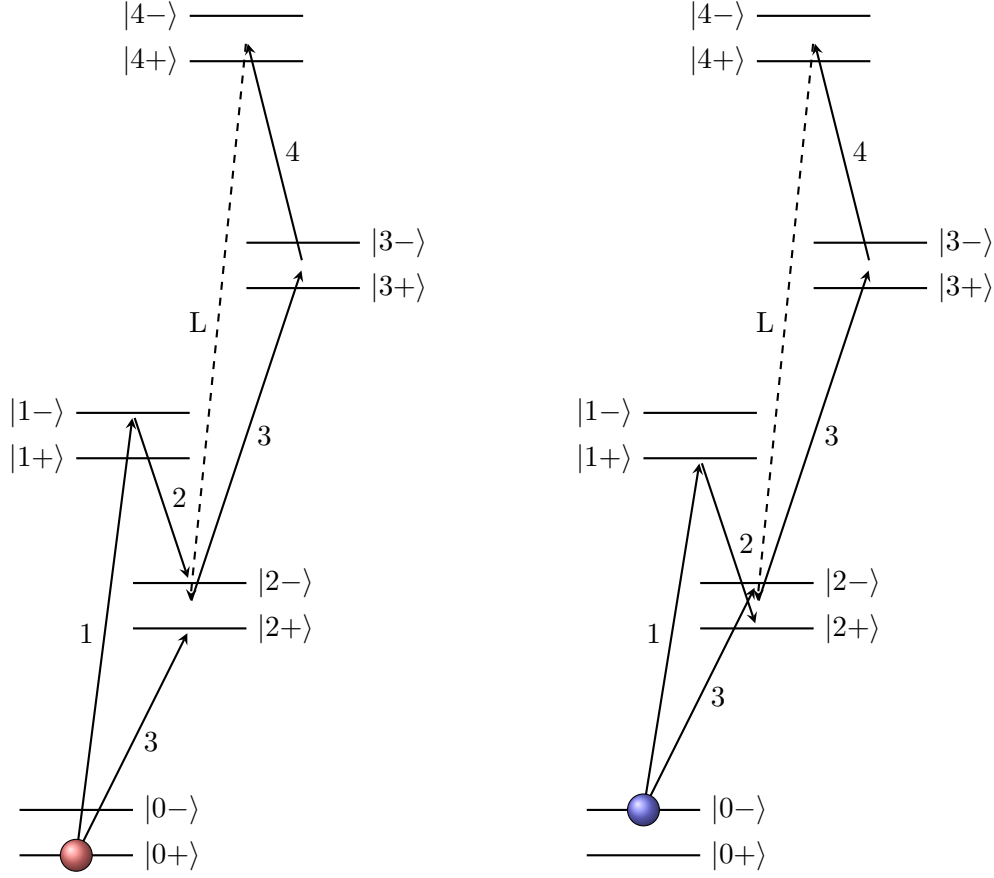


FIG. S3. Illustration of the (+)-cycle (left) and (-)-cycle (right). The initial state is denoted with a solid circle; the solid arrows indicate the microwave pulses connecting the rotational levels, and the dashed lines indicate the listen transitions. The numbers next to the solid arrows give the order of the microwave pulses in the sequence. The arrows starting and ending in between the sub-levels mean that the two transitions (3, 4, and L) are driven/detected simultaneously.

connecting states $|0-\rangle$, $|1+\rangle$, $|2\pm\rangle$, $|3\pm\rangle$, and $|4\pm\rangle$, will be denoted as (-)-cycle. These cycles are independent of each other and can be treated separately. The coupled cycles that start from the states $|1\mp\rangle$ will have exactly the same expressions but opposite phases, and the overall signal amplitude will be proportional to the population difference in pairs of states $|0\pm\rangle$ and $|1\mp\rangle$, as demonstrated in Ref. 1.

In the theoretical framework, we will use the following notations and assumptions:

- The three pulses in the pump cycle and two pulses in the probe cycle will be labeled with the index $n = 1 - 5$, showing their positions in the pulse sequence. The corre-

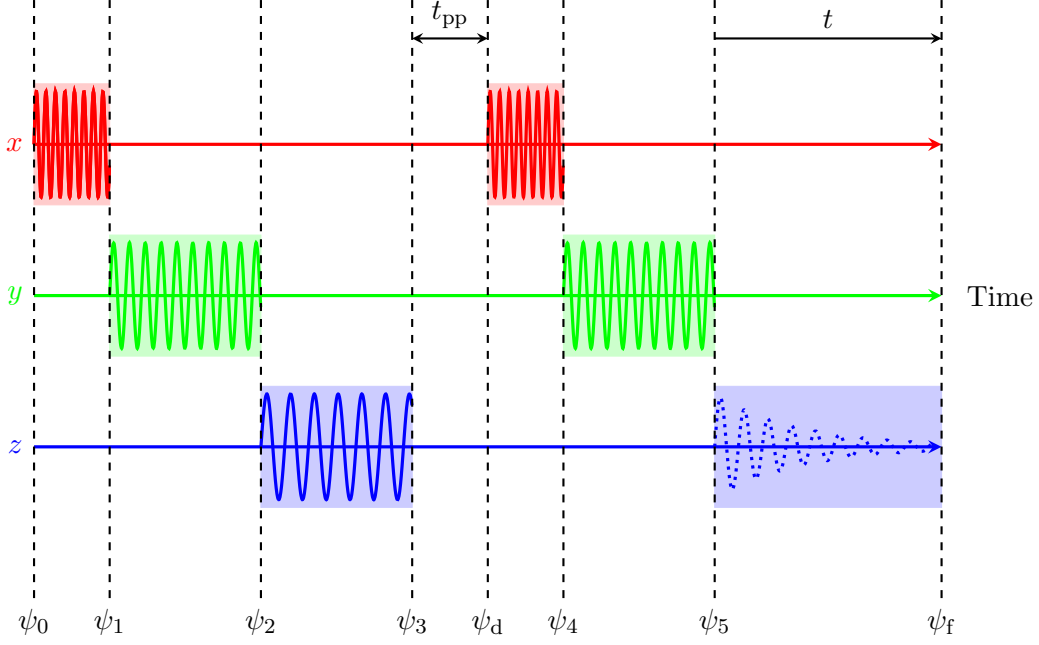


FIG. S4. Pulse scheme of the microwave pump-probe experiment in the time domain. Three axes (x, y, z) denote the three polarization directions in the laboratory frame. The colored solid sine-waves in boxes denote pulses, and the dotted decaying sine-curve on the right denote the listen signal. The vertical dashed lines denote the particular snapshots of the state (ψ) of the system, for which the explicit expressions are provided.

sponding duration, Rabi frequency, and carrier-envelope phase of the respective pulse will be denoted using τ_n , Ω_n , and φ_n .

- The Rabi oscillation amplitude of the wavefunction is expressed as:

$$\begin{cases} \mathcal{C}_n = \cos\left(\frac{\Omega_n \tau_n}{2}\right) \\ \mathcal{S}_n = \sin\left(\frac{\Omega_n \tau_n}{2}\right) . \end{cases} \quad (6)$$

- The accumulated oscillation phase at the n -th pulse of the (+)- or (-)-cycle at the $|k\pm\rangle$ state, composed of terms $\omega_{k'}\tau_{n'}$, will be defined as $q_{k\pm}^{(n\pm)}$, where the subscript denotes the state with $|\pm\rangle$ parity levels, and the superscript indicates the last passed pulse and the (\pm) -cycle.
- The frequency and transition dipole moment for a transition $|k\rangle \rightarrow |l\rangle$ will be denoted as $\omega_{kl} = \omega_l - \omega_k$ and $\boldsymbol{\mu}_{kl} = \langle k|\hat{\boldsymbol{\mu}}|l\rangle$. The transition-dipole moments are assumed to be real ($\boldsymbol{\mu}_{kl} = \boldsymbol{\mu}_{lk}$).

- The transition-dipole moments of the two intra-/interstate transitions are assumed to be equal, i.e., $\boldsymbol{\mu}_{k+l-} = \boldsymbol{\mu}_{k-l+} = \boldsymbol{\mu}_{kl}$ for the interstate and $\boldsymbol{\mu}_{k+l+} = \boldsymbol{\mu}_{k-l-} = \boldsymbol{\mu}_{kl}$ for the intrastate.
- The tunneling frequency in a given rotational state $|k\rangle$ is defined as

$$\omega_{kt} = \omega_{k-} - \omega_{k+} . \quad (7)$$

2. Wavefunction evolution

Here we outline the step-by-step evolution of the wavefunction throughout the microwave pump-probe experiment (see FIG. S4):

- The initial state of the system is

$$|\psi_0^\pm\rangle = |0\pm\rangle . \quad (8)$$

- The first pulse, driving the interstate transition $|0\pm\rangle \rightarrow |1\mp\rangle$ ($s_1 = +1$), puts the molecules in a superposition state

$$|\psi_1^\pm\rangle = \exp(-iq_{0\pm}^{(1\pm)})\mathcal{C}_1|0\pm\rangle - i \exp(-i\varphi_1 - iq_{1\mp}^{(1\pm)})\mathcal{S}_1|1\mp\rangle . \quad (9)$$

- After the second pulse, which excites the intrastate transition $|1\mp\rangle \rightarrow |2\mp\rangle$ ($s_2 = -1$), the system's state becomes

$$|\psi_2^\pm\rangle = \exp(-iq_{0\pm}^{(2\pm)})\mathcal{C}_1|0\pm\rangle - \exp(-i\varphi_1 + i\varphi_2 - iq_{2\mp}^{(2\pm)})\mathcal{S}_1\mathcal{S}_2|2\mp\rangle + \dots . \quad (10)$$

Hereinafter, “...” denotes the populated states that are not observable in the experiment.

- After the third pulse, which makes the intrastate transition $|0\pm\rangle \rightarrow |2\pm\rangle$ ($s_3 = +1$), the system is in the following superposition state

$$|\psi_3^\pm\rangle = -i \exp(-i\varphi_3 - iq_{2\pm}^{(3\pm)})\mathcal{C}_1\mathcal{S}_3|2\pm\rangle - \exp(-i\varphi_1 + i\varphi_2 - iq_{2\mp}^{(3\pm)})\mathcal{S}_1\mathcal{S}_2|2\mp\rangle + \dots . \quad (11)$$

- Following the three pumping pulses, the molecular system undergoes field-free evolution for a pump-probe delay time t_{pp} , reaching a delayed pumped state

$$\begin{aligned} |\psi_d^\pm\rangle = & -i \exp(-i\varphi_3 - i\omega_{2\pm}t_{pp} - iq_{2\pm}^{(3\pm)})\mathcal{C}_1\mathcal{S}_3|2\pm\rangle - \\ & - \exp(-i\varphi_1 + i\varphi_2 - i\omega_{2\mp}t_{pp} - iq_{2\mp}^{(3\pm)})\mathcal{S}_1\mathcal{S}_2|2\mp\rangle + \dots . \quad (12) \end{aligned}$$

- After the fourth pulse, which excites the intrastate transition $|2\pm\rangle \rightarrow |3\pm\rangle$ ($s_4 = +1$), the corresponding state of the system is

$$\begin{aligned}
|\psi_4^\pm\rangle = & -i \exp(-i\varphi_3 - i\omega_{2\pm}t_{\text{pp}} - iq_{2\pm}^{(4\pm)})\mathcal{C}_1\mathcal{S}_3\mathcal{C}_4|2\pm\rangle - \\
& - \exp(-i\varphi_1 + i\varphi_2 - i\omega_{2\mp}t_{\text{pp}} - iq_{2\mp}^{(4\pm)})\mathcal{S}_1\mathcal{S}_2\mathcal{C}_4|2\mp\rangle - \\
& - \exp(-i\varphi_3 - i\varphi_4 - i\omega_{2\pm}t_{\text{pp}} - iq_{3\pm}^{(4\pm)})\mathcal{C}_1\mathcal{S}_3\mathcal{S}_4|3\pm\rangle + \\
& + i \exp(-i\varphi_1 + i\varphi_2 - i\varphi_4 - i\omega_{2\mp}t_{\text{pp}} - iq_{3\mp}^{(4\pm)})\mathcal{S}_1\mathcal{S}_2\mathcal{S}_4|3\mp\rangle + \dots . \quad (13)
\end{aligned}$$

- After the fifth pulse, inducing the intrastate transition $|3\pm\rangle \rightarrow |4\pm\rangle$ ($s_5 = +1$), the system is in the state

$$\begin{aligned}
|\psi_5^\pm\rangle = & -i \exp(-i\varphi_3 - i\omega_{2\pm}t_{\text{pp}} - iq_{2\pm}^{(5\pm)})\mathcal{C}_1\mathcal{S}_3\mathcal{C}_4|2\pm\rangle - \\
& - \exp(-i\varphi_1 + i\varphi_2 - i\omega_{2\mp}t_{\text{pp}} - iq_{2\mp}^{(5\pm)})\mathcal{S}_1\mathcal{S}_2\mathcal{C}_4|2\mp\rangle + \\
& + i \exp(-i\varphi_3 - i\varphi_4 - i\varphi_5 - i\omega_{2\pm}t_{\text{pp}} - iq_{4\pm}^{(5\pm)})\mathcal{C}_1\mathcal{S}_3\mathcal{S}_4\mathcal{S}_5|4\pm\rangle + \\
& + \exp(-i\varphi_1 + i\varphi_2 - i\varphi_4 - i\varphi_5 - i\omega_{2\mp}t_{\text{pp}} - iq_{4\mp}^{(5\pm)})\mathcal{S}_1\mathcal{S}_2\mathcal{S}_4\mathcal{S}_5|4\mp\rangle + \dots . \quad (14)
\end{aligned}$$

- After all the microwave pulses, the final free evolving state of the molecular system with the time t is

$$\begin{aligned}
|\psi_f^\pm\rangle = & -i \exp(-i\varphi_3 - i\omega_{2\pm}t_{\text{pp}} - i\omega_{2\pm}t - iq_{2\pm}^{(5\pm)})\mathcal{C}_1\mathcal{S}_3\mathcal{C}_4|2\pm\rangle - \\
& - \exp(-i\varphi_1 + i\varphi_2 - i\omega_{2\mp}t_{\text{pp}} - i\omega_{2\mp}t - iq_{2\mp}^{(5\pm)})\mathcal{S}_1\mathcal{S}_2\mathcal{C}_4|2\mp\rangle + \\
& + i \exp(-i\varphi_3 - i\varphi_4 - i\varphi_5 - i\omega_{2\pm}t_{\text{pp}} - i\omega_{4\pm}t - iq_{4\pm}^{(5\pm)})\mathcal{C}_1\mathcal{S}_3\mathcal{S}_4\mathcal{S}_5|4\pm\rangle + \\
& + \exp(-i\varphi_1 + i\varphi_2 - i\varphi_4 - i\varphi_5 - i\omega_{2\mp}t_{\text{pp}} - i\omega_{4\mp}t - iq_{4\mp}^{(5\pm)})\mathcal{S}_1\mathcal{S}_2\mathcal{S}_4\mathcal{S}_5|4\mp\rangle + \dots . \quad (15)
\end{aligned}$$

3. Induced enantiomeric excess after the pump cycle

The enantiomeric excess (ee) in a rotational state $|k\rangle$ can be evaluated through the operator [1]

$$\hat{e}e_k = |R_k\rangle\langle R_k| - |S_k\rangle\langle S_k| = |k+\rangle\langle k-| + |k-\rangle\langle k+| , \quad (16)$$

where $|R_k\rangle$ and $|S_k\rangle$ are the non-stationary wavefunctions of the R and S enantiomer, respectively, in rotational state $|k\rangle$, defined as

$$\begin{cases} |R_k\rangle = \frac{1}{\sqrt{2}}(|k+\rangle + |k-\rangle) , \\ |S_k\rangle = \frac{1}{\sqrt{2}}(|k+\rangle - |k-\rangle) . \end{cases} \quad (17)$$

Applying Equation 16 for rotational state $|2\rangle$ and wavefunctions $|\psi_d^\pm\rangle$ (Equation 12), we can evaluate the ee induced in state $|2\rangle$ after the pump sequence. By representing the state $|\psi_d^\pm\rangle$ as

$$|\psi_d^\pm\rangle = c_{2+}^\pm |2+\rangle + c_{2-}^\pm |2-\rangle + \dots \quad (18)$$

with coefficients

$$\begin{cases} c_{2+}^+ = -i \exp(-i\varphi_3 - i\omega_{2+}t_{pp} - iq_{2+}^{(3+)}) \mathcal{C}_1 \mathcal{S}_3 , \\ c_{2-}^+ = -\exp(-i\varphi_1 + i\varphi_2 - i\omega_{2-}t_{pp} - iq_{2-}^{(3+)}) \mathcal{S}_1 \mathcal{S}_2 , \end{cases} \quad (19)$$

for the (+)-cycle and

$$\begin{cases} c_{2+}^- = -\exp(-i\varphi_1 + i\varphi_2 - i\omega_{2+}t_{pp} - iq_{2+}^{(3-)}) \mathcal{S}_1 \mathcal{S}_2 , \\ c_{2-}^- = -i \exp(-i\varphi_3 - i\omega_{2-}t_{pp} - iq_{2-}^{(3-)}) \mathcal{C}_1 \mathcal{S}_3 , \end{cases} \quad (20)$$

for the (-)-cycle, we get the following result for the ee :

$$ee_2^{(\pm)} = \langle \psi_d^\pm | \hat{e}e_2 | \psi_d^\pm \rangle = 2\text{Re} \left((c_{2-}^\pm)^* c_{2+}^\pm \right) . \quad (21)$$

By substituting the coefficients from Equation 19 into Equation 21, we get the result for the (+)-cycle:

$$\begin{aligned} ee_2^{(+)} &= 2\mathcal{C}_1 \mathcal{S}_1 \mathcal{S}_2 \mathcal{S}_3 \text{Re} \left[i \exp(+i\varphi_1 - i\varphi_2 + i\omega_{2-}t_{pp} + iq_{2-}^{(3+)} - i\varphi_3 - i\omega_{2+}t_{pp} - iq_{2+}^{(3+)}) \right] \\ &= -\sin(\Omega_1 \tau_1) \sin\left(\frac{\Omega_2 \tau_2}{2}\right) \sin\left(\frac{\Omega_3 \tau_3}{2}\right) \sin(\omega_{2t} t_{pp} + \varphi_1 - \varphi_2 - \varphi_3 + \Delta q_2^{3+}) , \end{aligned} \quad (22)$$

where $\omega_{2t} t_{pp}$ is given by Equation 7 and $\Delta q_2^+ = q_{2-}^{(3+)} - q_{2+}^{(3+)}$.

Similarly, substituting the coefficients from Equation 20 into Equation 21 yields the result for the (-)-cycle:

$$\begin{aligned} ee_2^{(-)} &= -2\mathcal{C}_1 \mathcal{S}_1 \mathcal{S}_2 \mathcal{S}_3 \text{Re} \left[i \exp(i\varphi_3 + i\omega_{2-}t_{pp} + iq_{2-}^{(3-)} - i\varphi_1 + i\varphi_2 - i\omega_{2+}t_{pp} - iq_{2+}^{(3-)}) \right] \\ &= \sin(\Omega_1 \tau_1) \sin\left(\frac{\Omega_2 \tau_2}{2}\right) \sin\left(\frac{\Omega_3 \tau_3}{2}\right) \sin(\omega_{2t} t_{pp} - \varphi_1 + \varphi_2 + \varphi_3 + \Delta q_2^{3-}) , \end{aligned} \quad (23)$$

where $\Delta q_2^{3-} = q_{2-}^{(3-)} - q_{2+}^{(3-)}$.

Thereby, to reach maximal enantiomeric excess in each cycle (Equations 22 and 23), the first pulse should be a $\pi/2$ -pulse ($\Omega_1\tau_1 = \pi/2$), while the second and third pulses should be π -pulses ($\Omega_2\tau_2 = \Omega_3\tau_3 = \pi$).

4. Listen signal in the pump-probe scheme

The observed emission signal arises from the induced dipole moment oscillating between two given states coherently. For the two interstate listen transitions, namely $|4\pm\rangle \rightarrow |2\mp\rangle$, the induced signal can be described with a polarization operator

$$\hat{\mathbf{P}}_{4\pm \rightarrow 2\mp} = \boldsymbol{\mu}_{42} (|4\pm\rangle\langle 2\mp| + |2\mp\rangle\langle 4\pm|) . \quad (24)$$

Similar to the ee in the $|2\pm\rangle$ states (Equation 21), the macroscopic polarization induced in a given (+)- or (-)-cycle is thus expressed by:

$$\mathbf{P}_{4\pm \rightarrow 2\mp}^{(\pm)} = \langle \psi_f^\pm | \hat{\mathbf{P}}_{4\pm \rightarrow 2\mp} | \psi_f^\pm \rangle = 2\boldsymbol{\mu}_{42} \cdot \text{Re} \left((c_{4\pm}^\pm)^* c_{2\mp}^\pm \right) , \quad (25)$$

where the coefficients are given in the representation of the final wavefunction $\psi_f^\pm = c_{2+}^\pm |2+\rangle + c_{2-}^\pm |2-\rangle + c_{4+}^\pm |4+\rangle + c_{4-}^\pm |4-\rangle$ in Equation 15, which are

$$\begin{cases} c_{2+}^+ = -i \exp(-i\varphi_3 - i\omega_{2+}t_{\text{pp}} - i\omega_{2+}t - iq_{2+}^{(5+)}) \mathcal{C}_1 \mathcal{S}_3 \mathcal{C}_4 , \\ c_{2-}^+ = -\exp(-i\varphi_1 + i\varphi_2 - i\omega_{2-}t_{\text{pp}} - i\omega_{2-}t - iq_{2-}^{(5+)}) \mathcal{S}_1 \mathcal{S}_2 \mathcal{C}_4 , \\ c_{4+}^+ = i \exp(-i\varphi_3 - i\varphi_4 - i\varphi_5 - i\omega_{2+}t_{\text{pp}} - i\omega_{4+}t - iq_{4+}^{(5+)}) \mathcal{C}_1 \mathcal{S}_3 \mathcal{S}_4 \mathcal{S}_5 , \\ c_{4-}^+ = \exp(-i\varphi_1 + i\varphi_2 - i\varphi_4 - i\varphi_5 - i\omega_{2-}t_{\text{pp}} - i\omega_{4-}t - iq_{4-}^{(5+)}) \mathcal{S}_1 \mathcal{S}_2 \mathcal{S}_4 \mathcal{S}_5 . \end{cases} \quad (26)$$

for the (+)-cycle, and

$$\begin{cases} c_{2+}^- = -\exp(-i\varphi_1 + i\varphi_2 - i\omega_{2+}t_{\text{pp}} - i\omega_{2+}t - iq_{2+}^{(5-)}) \mathcal{S}_1 \mathcal{S}_2 \mathcal{C}_4 , \\ c_{2-}^- = -i \exp(-i\varphi_3 - i\omega_{2-}t_{\text{pp}} - i\omega_{2-}t - iq_{2-}^{(5-)}) \mathcal{C}_1 \mathcal{S}_3 \mathcal{C}_4 , \\ c_{4+}^- = \exp(-i\varphi_1 + i\varphi_2 - i\varphi_4 - i\varphi_5 - i\omega_{2+}t_{\text{pp}} - i\omega_{4+}t - iq_{4+}^{(5-)}) \mathcal{S}_1 \mathcal{S}_2 \mathcal{S}_4 \mathcal{S}_5 , \\ c_{4-}^- = i \exp(-i\varphi_3 - i\varphi_4 - i\varphi_5 - i\omega_{2-}t_{\text{pp}} - i\omega_{4-}t - iq_{4-}^{(5-)}) \mathcal{C}_1 \mathcal{S}_3 \mathcal{S}_4 \mathcal{S}_5 . \end{cases} \quad (27)$$

for the (-)-cycle, respectively.

In the case of the (+)-cycle, we will obtain the two following expressions for the signal at the two components of the interstate listen transition. For the higher frequency component ($|4-\rangle \rightarrow |2+\rangle$), we get

$$\begin{aligned}
\mathbf{P}_{4-\rightarrow 2+}^{(+)} &= \langle \psi_f^+ | \hat{\mathbf{P}}_{4-\rightarrow 2+} | \psi_f^+ \rangle = 2\boldsymbol{\mu}_{42} \cdot \text{Re} \left((c_{4-}^+)^* c_{2+}^+ \right) = \\
&= -2\boldsymbol{\mu}_{42} \mathcal{C}_1 \mathcal{S}_1 \mathcal{S}_2 \mathcal{S}_3 \mathcal{C}_4 \mathcal{S}_4 \mathcal{S}_5 \times \\
&\times \text{Re} \left(i \exp \left(i\omega_{2+4-}t + i\omega_{2t}t_{\text{pp}} + i\varphi_1 - i\varphi_2 - i\varphi_3 + i\varphi_4 + i\varphi_5 + i\Delta q_{2+4-}^{(5+)} \right) \right) = \\
&= \underbrace{\frac{\boldsymbol{\mu}_{42}}{2} \sin(\Omega_1\tau_1) \sin\left(\frac{\Omega_2\tau_2}{2}\right) \sin\left(\frac{\Omega_3\tau_3}{2}\right) \sin(\Omega_4\tau_4) \sin\left(\frac{\Omega_5\tau_5}{2}\right)}_{\mathbf{A}_{42}} \times \\
&\times \sin \left(\omega_{2+4-}t + \omega_{2t}t_{\text{pp}} + \varphi_1 - \varphi_2 - \varphi_3 + \varphi_4 + \varphi_5 + \Delta q_{2+4-}^{(5+)} \right), \quad (28)
\end{aligned}$$

where $\Delta q_{2+4-}^{(5+)} = q_{4-}^{(5+)} - q_{2+}^{(5+)}$ and \mathbf{A}_{42} is the total amplitude of the signal. The conditions for maximizing \mathbf{A}_{42} are that the first and the fourth pulse are $\pi/2$ -pulses, while all the others are π -pulses. Similarly, for the lower frequency component ($|4+\rangle \rightarrow |2-\rangle$), we have

$$\begin{aligned}
\mathbf{P}_{4+\rightarrow 2-}^{(+)} &= \langle \psi_f^+ | \hat{\mathbf{P}}_{4+\rightarrow 2-} | \psi_f^+ \rangle = 2\boldsymbol{\mu}_{42} \cdot \text{Re} \left((c_{4+}^+)^* c_{2-}^+ \right) = \\
&= 2\boldsymbol{\mu}_{42} \mathcal{C}_1 \mathcal{S}_1 \mathcal{S}_2 \mathcal{S}_3 \mathcal{C}_4 \mathcal{S}_4 \mathcal{S}_5 \times \\
&\times \text{Re} \left(i \exp \left(i\omega_{2-4+}t - i\omega_{2t}t_{\text{pp}} - i\varphi_1 + i\varphi_2 + i\varphi_3 + i\varphi_4 + i\varphi_5 + i\Delta q_{2-4+}^{(5+)} \right) \right) = \\
&= -\underbrace{\frac{\boldsymbol{\mu}_{42}}{2} \sin(\Omega_1\tau_1) \sin\left(\frac{\Omega_2\tau_2}{2}\right) \sin\left(\frac{\Omega_3\tau_3}{2}\right) \sin(\Omega_4\tau_4) \sin\left(\frac{\Omega_5\tau_5}{2}\right)}_{\mathbf{A}_{42}} \times \\
&\times \sin \left(\omega_{2-4+}t - \omega_{2t}t_{\text{pp}} - \varphi_1 + \varphi_2 + \varphi_3 + \varphi_4 + \varphi_5 + \Delta q_{2-4+}^{(5+)} \right), \quad (29)
\end{aligned}$$

where $\Delta q_{2-4+}^{(5+)} = q_{4+}^{(5+)} - q_{2-}^{(5+)}$.

In the case of the (-)-cycle, we can do the same derivation. For the higher frequency component ($|4-\rangle \rightarrow |2+\rangle$), we get

$$\begin{aligned}
\mathbf{P}_{4-\rightarrow 2+}^{(-)} &= \langle \psi_f^- | \hat{\mathbf{P}}_{4-\rightarrow 2+} | \psi_f^- \rangle = 2\boldsymbol{\mu}_{42} \cdot \text{Re} \left((c_{4-}^-)^* c_{2+}^- \right) = \\
&= -2\boldsymbol{\mu}_{42} \mathcal{C}_1 \mathcal{S}_1 \mathcal{S}_2 \mathcal{S}_3 \mathcal{C}_4 \mathcal{S}_4 \mathcal{S}_5 \times \\
&\times \text{Re} \left(i \exp \left(i\omega_{2+4-t} + i\omega_{2t} t_{\text{pp}} - i\varphi_1 + i\varphi_2 + i\varphi_3 + i\varphi_4 + i\varphi_5 + i\Delta q_{2+4-}^{(5-)} \right) \right) = \\
&= \underbrace{\frac{\boldsymbol{\mu}_{42}}{2} \sin(\Omega_1 \tau_1) \sin\left(\frac{\Omega_2 \tau_2}{2}\right) \sin\left(\frac{\Omega_3 \tau_3}{2}\right) \sin(\Omega_4 \tau_4) \sin\left(\frac{\Omega_5 \tau_5}{2}\right)}_{\mathbf{A}_{42}} \times \\
&\times \sin \left(\omega_{2+4-t} + \omega_{2t} t_{\text{pp}} - \varphi_1 + \varphi_2 + \varphi_3 + \varphi_4 + \varphi_5 + \Delta q_{2+4-}^{(5-)} \right), \quad (30)
\end{aligned}$$

where $\Delta q_{2+4-}^{(5-)} = q_{4-}^{(5-)} - q_{2+}^{(5-)}$. For the lower frequency component ($|4+\rangle \rightarrow |2-\rangle$) of the $(-)$ -cycle, we obtain

$$\begin{aligned}
\mathbf{P}_{4+\rightarrow 2-}^{(-)} &= \langle \psi_f^- | \hat{\mathbf{P}}_{4+\rightarrow 2-} | \psi_f^- \rangle = 2\boldsymbol{\mu}_{42} \cdot \text{Re} \left((c_{4+}^-)^* c_{2-}^- \right) = \\
&= 2\boldsymbol{\mu}_{42} \mathcal{C}_1 \mathcal{S}_1 \mathcal{S}_2 \mathcal{S}_3 \mathcal{C}_4 \mathcal{S}_4 \mathcal{S}_5 \times \\
&\times \text{Re} \left(i \exp \left(i\omega_{2-4+t} - i\omega_{2t} t_{\text{pp}} + i\varphi_1 - i\varphi_2 - i\varphi_3 + i\varphi_4 + i\varphi_5 + i\Delta q_{2-4+}^{(5-)} \right) \right) = \\
&= \underbrace{\frac{\boldsymbol{\mu}_{42}}{2} \sin(\Omega_1 \tau_1) \sin\left(\frac{\Omega_2 \tau_2}{2}\right) \sin\left(\frac{\Omega_3 \tau_3}{2}\right) \sin(\Omega_4 \tau_4) \sin\left(\frac{\Omega_5 \tau_5}{2}\right)}_{\mathbf{A}_{42}} \times \\
&\times \sin \left(\omega_{2-4+t} - \omega_{2t} t_{\text{pp}} + \varphi_1 - \varphi_2 - \varphi_3 + \varphi_4 + \varphi_5 + \Delta q_{2-4+}^{(5-)} \right), \quad (31)
\end{aligned}$$

where $\Delta q_{2-4+}^{(5+)} = q_{4+}^{(5+)} - q_{2-}^{(5+)}$.

The total signal, however, in the case of the $(+)$ -cycle will be a combination of two induced signals (Equations 28 and 29), namely,

$$\begin{aligned}
\mathbf{P}_{4\rightarrow 2}^{(+)}(t) &= \mathbf{P}_{4-\rightarrow 2+}^{(+)} + \mathbf{P}_{4+\rightarrow 2-}^{(+)} = \\
&= \underbrace{\mathbf{P}_{\text{M3WM}}^{(+)}(t)}_{2\mathbf{A}_{42} \cos(\omega_{24} t + \varphi_4 + \varphi_4 + \Delta q_{24}^{(5+)})} \times \\
&\times \underbrace{\sin(\Delta\omega_{24} t + \omega_{2t} t_{\text{pp}} + \varphi_1 - \varphi_2 - \varphi_3 + \Delta\Delta q_{24}^{(5+)})}_{W_t^{(+)}(t)} = \\
&= \mathbf{P}_{\text{M3WM}}^{(+)}(t) \times W_t^{(+)}(t), \quad (32)
\end{aligned}$$

where $\omega_{24} = (\omega_{2-4+} + \omega_{2+4-})/2$ is the mid-frequency of the $|4\rangle \rightarrow |2\rangle$ transition, $\Delta q_{24}^{(5+)} = (\Delta q_{2+4-}^{(5+)} + \Delta q_{2-4+}^{(5+)})/2$, $\Delta\omega_{24} = (\omega_{2-4+} - \omega_{2+4-})/2$ is the mean tunneling frequency in states

$|2\rangle$ and $|4\rangle$, and $\Delta\Delta q_{24}^{(5+)} = (\Delta q_{2+4-}^{(5+)} - \Delta q_{2-4+}^{(5+)})/2$. Similarly, for the $(-)$ -cycle, the observed total signal will be

$$\begin{aligned}
\mathbf{P}_{4\rightarrow 2}^{(-)}(t) &= \mathbf{P}_{4\rightarrow 2+}^{(-)} + \mathbf{P}_{4\rightarrow 2-}^{(-)} = \\
&= \overbrace{2\mathbf{A}_{42} \sin(\omega_{24}t + \varphi_4 + \varphi_4 + \Delta q_{24}^{(5-)})}^{\mathbf{P}_{\text{M3WM}}^{(-)}(t)} \times \\
&\times \underbrace{\cos(\Delta\omega_{24}t + \omega_{2t}t_{\text{pp}} - \varphi_1 + \varphi_2 + \varphi_3 + \Delta\Delta q_{24}^{(5-)})}_{W_t^{(-)}(t)} = \\
&= \mathbf{P}_{\text{M3WM}}^{(-)}(t) \times W_t^{(-)}(t), \quad (33)
\end{aligned}$$

$\Delta q_{24}^{(5-)} = (\Delta q_{2+4-}^{(5-)} + \Delta q_{2-4+}^{(5-)})/2$ and $\Delta\Delta q_{24}^{(5-)} = (\Delta q_{2+4-}^{(5-)} - \Delta q_{2-4+}^{(5-)})/2$. In both these cases (Equations 32 and 33), the final signal is composed of the main signal ($\mathbf{P}_{\text{M3WM}}^{(\pm)}(t)$) at the mean frequency of the unsplit rotational transition (ω_{24}) and the envelope motion ($W_t^{(\pm)}(t)$), that periodically stops the signal $\mathbf{P}_{\text{M3WM}}^{(\pm)}$, and then restarts it with the opposite phase. The repetition frequency of this motion is the mean tunneling frequency between the two states ($\Delta\omega_{24}$). The signal $\mathbf{P}_{\text{M3WM}}^{(\pm)}$ represents a pure microwave three-wave mixing (M3WM) signal for a given chiral state, whilst the coherent beating function $W_t^{(\pm)}$ represents the tunneling motion of this chiral wavepacket from one potential well to another.

II. Supplementary experimental details

A. Experimental microwave pump-probe scheme

The level diagram of 3-fluorobenzyl alcohol used in the pump-probe experiments is shown in FIG. S5. It includes both the $(+)$ - and $(-)$ -cycles (see FIG. S3), which begins from the $|0_{00}^+\rangle$ and $|0_{00}^-\rangle$ states, respectively. The rotational level is labeled with $|J_{K_a K_c}\rangle$, where J is the total angular momentum quantum number, and K_a and K_c are projections of this momentum onto the a - and c -axes in the inertial principal axis system (PAS). The two tunneling states are marked with the \pm parity. As the tunneling motion inverts the electric dipole-moment component along the c -principal axis of the molecule, μ_c -type transitions ($|0_{00}\rangle \rightarrow |1_{10}\rangle$ and $|1_{01}\rangle \rightarrow |2_{11}\rangle$) are allowed between tunneling substates of opposite parity (f^\mp : $|+\rangle \rightarrow |-\rangle$ and f^\pm : $|-\rangle \rightarrow |+\rangle$), which are known as interstate transitions. The two interstate transition components are approximately separated by $2\varepsilon_\pm/h$ in frequency, which

is about 1.64 MHz. The μ_a - and μ_b -type transitions are intrastate transitions ($|+\rangle \rightarrow |+\rangle$ and $|-\rangle \rightarrow |-\rangle$), where the splittings are very small for 3-fluorobenzyl alcohol. As a result, both components of the intrastate transitions can be excited using single frequencies.

By starting from the interstate transitions f_1^\mp and f_1^\pm , the (+)- and (-)-pumping sub-cycles can be separated, avoiding the interference between them. In the probe cycle, the excitation of the intrastate transitions f_4 and f_5 simultaneously drives both probing sub-cycles, giving rise to a response signal at the listen frequencies of f_L^\mp and f_L^\pm , which can be observed as frequency beats in the time domain. In the main text, we focus on experiments

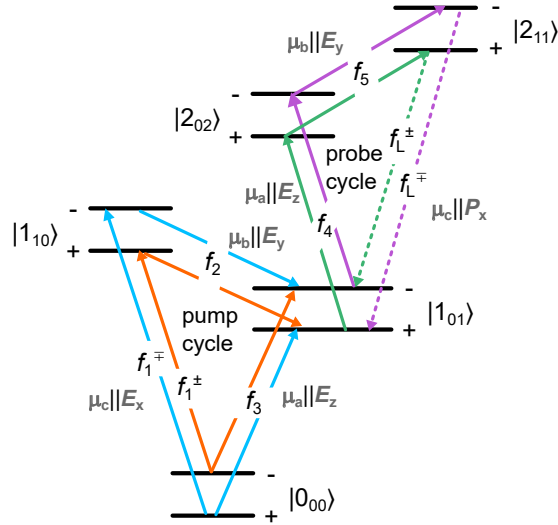


FIG. S5. Energy levels of the rotational states of 3-fluorobenzyl alcohol used for the microwave pump-probe experiment. Each state is labeled with the rotational level $|J_{K_a K_c}\rangle$ and the associated parity \pm . Transitions are denoted as f_i with i being the index of the microwave pulse in the experimental sequence. The interstate transition components ($|+\rangle \rightarrow |-\rangle$ and $|-\rangle \rightarrow |+\rangle$) are associated with different frequencies (f_1^\mp and f_1^\pm), and the intrastate transition components ($|+\rangle \rightarrow |+\rangle$ and $|-\rangle \rightarrow |-\rangle$) can be excited using single frequencies (f_i). For each transition, the corresponding dipole-moment component in the molecular frame and the polarization direction of the microwave field in the laboratory frame are indicated using $\mu_\alpha \parallel \mathbf{E}_\beta$ ($\alpha = a, b, c$; $\beta = x, y, z$). The spatial M_J degeneracies of the transitions are omitted for the sake of clarity. ($f_1^\pm = 3966.18$ MHz, $f_1^\mp = 3967.82$ MHz, $f_2 = 1894.35$ MHz, $f_3 = 2072.65$ MHz, $f_4 = 4093.31$ MHz, $f_5 = 2293.06$ MHz, $f_L^\pm = 6385.55$ MHz, and $f_L^\mp = 6387.18$ MHz).

using the (+)-cycle, while here we also present results from the (-)-cycle.

B. Sample preparation and experimental setup

A commercially available sample of 3-fluorobenzyl alcohol (chemical purity: 98%) is purchased from Fisher Scientific and used without additional purification. The sample is liquid at room temperature and reaches a vapor pressure of approximately 30 mbar when heated to 104–105 °C. It is placed into a sample reservoir, which is part of a home-built stainless-steel nozzle modified from a General Valve (Series 9), and maintained at 100 °C throughout the experiments. The nozzle reservoir is situated inside the spectrometer chamber with a background vacuum of $\sim 10^{-6}$ mbar. The sample vapor is diluted into neon carrier gas at a backing pressure of 3 bar and supersonically expanded into the vacuum chamber via the solenoid valve. This cools down the molecules to a rotational temperature (T_{rot}) of about 1 K. After an expansion time of 1100 μs , molecules in the jet expansion reach the interaction region with the microwave radiation.

As sketched in FIG. S6, the Fourier transform microwave spectrometer is equipped with an arbitrary waveform generator (AWG) to generate rectangular microwave pulses, which is operated in a dual-channel mode with a maximum frequency of up to 6 GHz. The produced pulses can be fed through different microwave amplifiers for power amplification. Three microwave amplifiers are used in this study, including a 50 W solid-state amplifier (SSA), a 3 W SSA, and a 300 W traveling-wave tube amplifier (TWTA). Two dual-polarization horn antennae are placed perpendicularly inside the vacuum chamber to transmit microwave fields in dedicated polarization directions.

The microwave pulses interact with molecules in the jet expansion, aligning their electric-dipole moments and resulting in a macroscopic polarization in the molecular ensemble. After the excitation, the decay of the macroscopic polarization is measured as a function of time using a third horn antenna on the other side of the chamber. As illustrated in the schematic of the experimental setup, the molecular beam and the microwave fields propagate in perpendicular directions, thereby preventing Doppler frequency shifting during the measurement. The FID signals are recorded for 40 μs , accumulated, and saved on a fast oscilloscope. The solenoid valve is pulsed at 8 Hz, and each gas jet is repeatedly polarized eight times, leading to an overall 64 Hz repetition rate of the experiment. The averaged time-

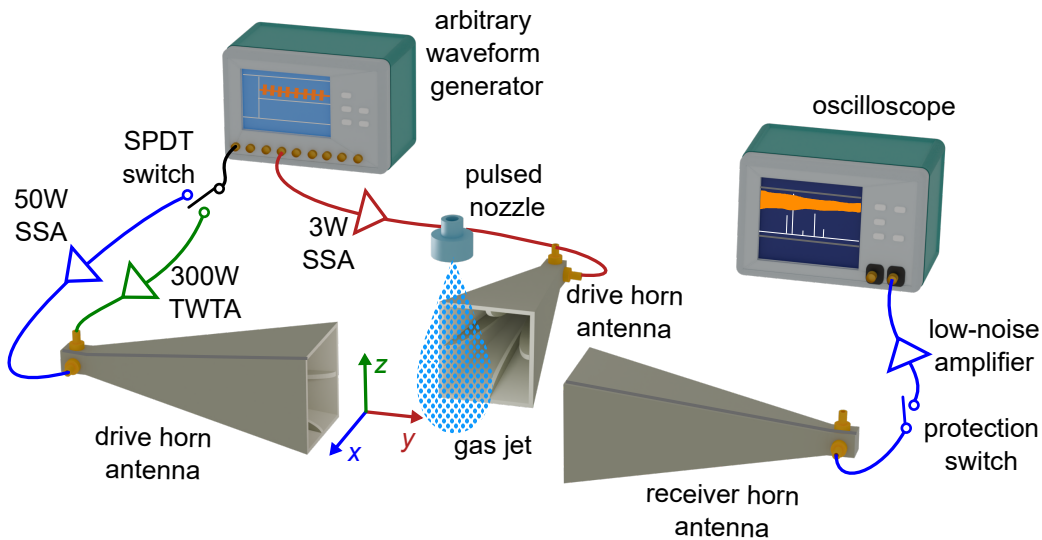


FIG. S6. Schematic of the Fourier transform microwave (FTMW) spectrometer COMPACT. The chemical compound is held in the reservoir nozzle. Its vapor, diluted into neon gas, is introduced into the spectrometer chamber via a supersonic expansion. The orifice of the solenoid valve is about 1 mm. In the excitation circuit, the spectrometer is equipped with an arbitrary waveform generator (AWG), two dual-polarization horn antennae, and multiple microwave amplifiers. The arbitrary waveform generator works in a two-channel mode. The sample rate of each channel is 12 GSa/s, which allows for generating frequencies up to 6 GHz. The output from channel 1 can be further divided via a single-pole-double-throw (SPDT) PIN diode switch so that microwave pulses can be broadcast into different polarization directions. To transmit microwave fields into designated directions (E_x , E_y , and E_z), two drive dual-polarization horn antennae are installed perpendicularly. Prior to the signal transmission, microwave pulses in different paths are power amplified with dedicated microwave amplifiers, which are a 50 W solid-state amplifier (SSA), a 3 W SSA, and a 300 W traveling-wave tube amplifier. After the interactions between microwave pulses and jet-cooled molecules, the free induction decay (FID) of the macroscopic molecular response is collected using a dual-polarization receiver horn antenna, averaged, and saved on a fast oscilloscope. All the frequency signals in the excitation and detection circuit are referenced to the same system clock, a 10 MHz rubidium frequency standard. (This figure is a copy of FIG. 2b of the main text, repeated here for completeness.)

domain FIDs are fast Fourier transformed into the frequency domain to obtain the signal intensities and phases with a Kaiser window function ($\beta = 9.5$). The spectral resolution is 25 kHz with a frequency accuracy of 10 kHz, and the peak widths at full-width-half-maximum (FWHM) are about 60 kHz. To visualize the signals at given frequencies in the time domain, the FIDs are filtered using a bandpass Butterworth filter (6th-order) with a bandwidth of 60 kHz.

C. Preparation of microwave fields

As described in Equations 28–31, the amplitude of the induced signals at the listen transitions depends on the conditions of the microwave radiation fields. The maximum coherence and amplitude of the listen signal are achieved when microwave pulses #1 and #4 are Rabi $\pi/2$ -pulses and pulses #2 and #3, and #5 are π -pulses. The $\pi/2$ and π conditions are referred to the Rabi flip angle, which is defined as

$$\Theta = \Omega \cdot \tau = \frac{\boldsymbol{\mu} \cdot \mathbf{E}}{\hbar} \cdot \tau \quad (34)$$

where Ω is the Rabi frequency (see Equation 4) and τ is the duration of the microwave pulse. In general, a $\pi/2$ -pulse creates a 50:50 superposition between two states, while a π -pulse inverts the population between them.

Before conducting the pump-probe experiments, it is necessary to measure Rabi oscillation curves, also known as nutation curves, for rotational transitions in the level scheme. Such nutation curves represent Rabi cycles as a function of pulse duration, which will allow us to adjust excitation conditions by varying the pulse durations in the following pump-probe experiments. According to the magnitudes of the dipole-moment components of 3-fluorobenzyl alcohol, which are calculated to be $|\mu_a| = 0.1$ D, $|\mu_b| = 2.6$ D, and $|\mu_c| = 0.5$ D at the MP2/6-311++G** level of theory [3], transitions are designated to microwave amplifiers with appropriate power. This ensures that the microwave pulse duration is on the order of microseconds or sub-microseconds, which is practical for the electronics and minimizes decoherence in the excitation process. In this study, spatial M_J -degeneracy is omitted for clarity. The observed nutation curves result from contributions from all M_J -substates of the transitions.

For intrastate transitions (f_2 – f_5), the tunneling components can be excited simultane-

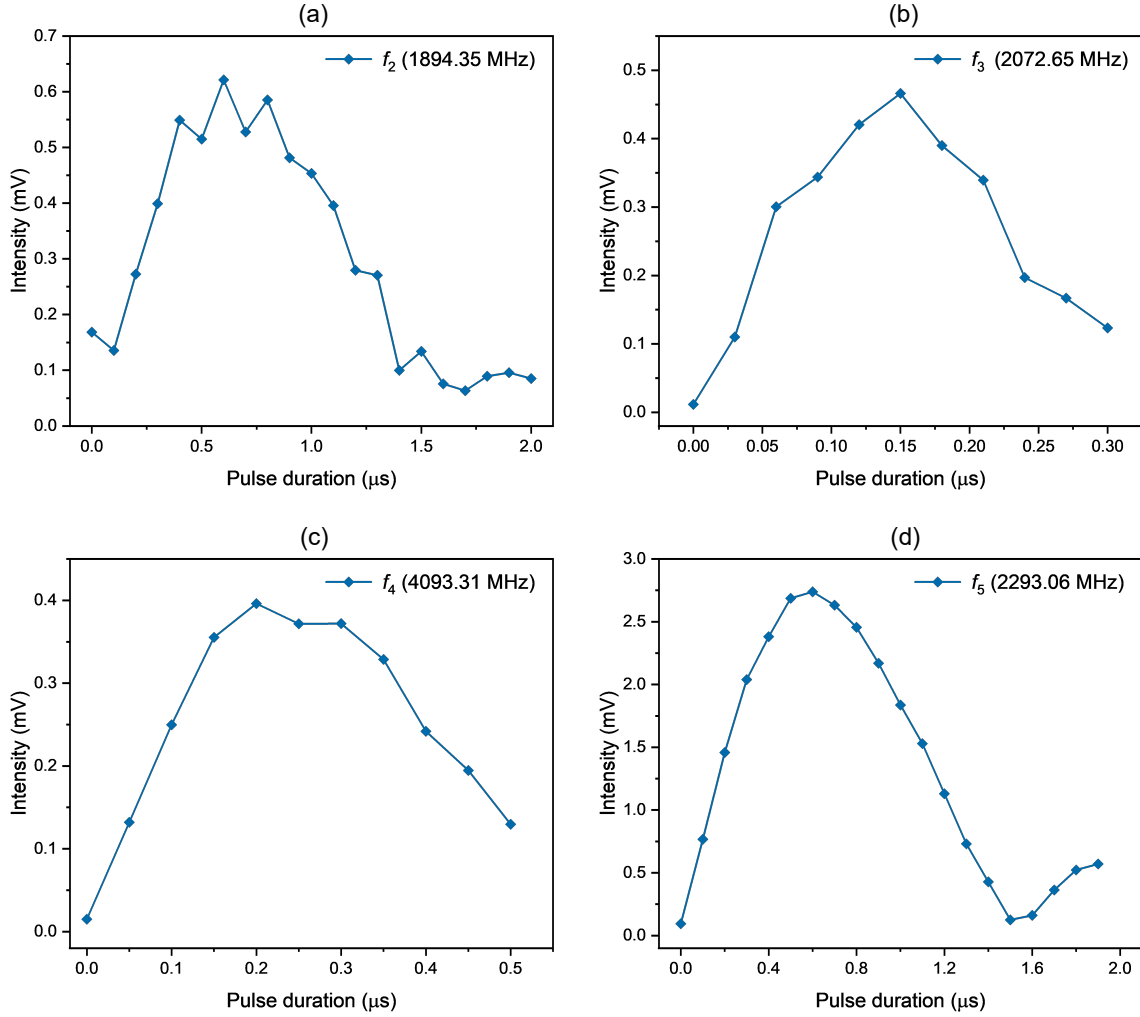


FIG. S7. Nutation curves for the intrastate transitions f_2 – f_5 (a–d) in the microwave pulse sequence as a function of pulse duration (in μs). The excitation and detection are performed in the same polarization direction. Each point on the curves is from an accumulation of 15000 FIDs.

ously using the same resonant frequency (see Section II A). The recorded nutation curves are presented in FIG. S7. In each measurement, the excitation and detection are conducted in the same polarization direction. Microwave pulses of f_2 and f_5 and pulses of f_3 and f_4 are fed through a 3 W solid-state amplifier and a 300 W traveling-wave tube amplifier, respectively. For the interstate transition f_1 , as the tunneling doublet is only separated by approximately 1.64 MHz, which is close to the spectral bandwidth of the microwave pulse, it is experimentally difficult to solely excite one single component. Therefore, the nutation curves are performed at the center frequency (FIG. S8a), where both transition components

are symmetrically detuned by Δ , and at the respective resonant frequencies (FIGs. S8b and S8c), where one component is on resonance and the other one is detuned by 2Δ . See Section IA for an explanation of the detuning effect.

As shown in FIG. S8, when excited at the center frequency, both transitions undergo approximately identical Rabi oscillations, with a $\pi/2$ duration of about $0.5 \mu\text{s}$. However, when the excitation occurs at individual resonant frequencies, the two components exhibit distinct Rabi oscillatory behaviors, with the $\pi/2$ duration being $0.4 \mu\text{s}$ for the resonant component and $0.3 \mu\text{s}$ for the detuned component. At $0.6 \mu\text{s}$, when the detuned component reaches the π condition, the intensities of the two components exhibit the highest contrast, approximately 10:1. This allows us to separate the two pump sub-cycles in the experiment. Note that these durations correspond to the effective conditions averaged over M_J -substates of the corresponding transitions [4], Overall, the measured pulse conditions are summarized in Table S1.

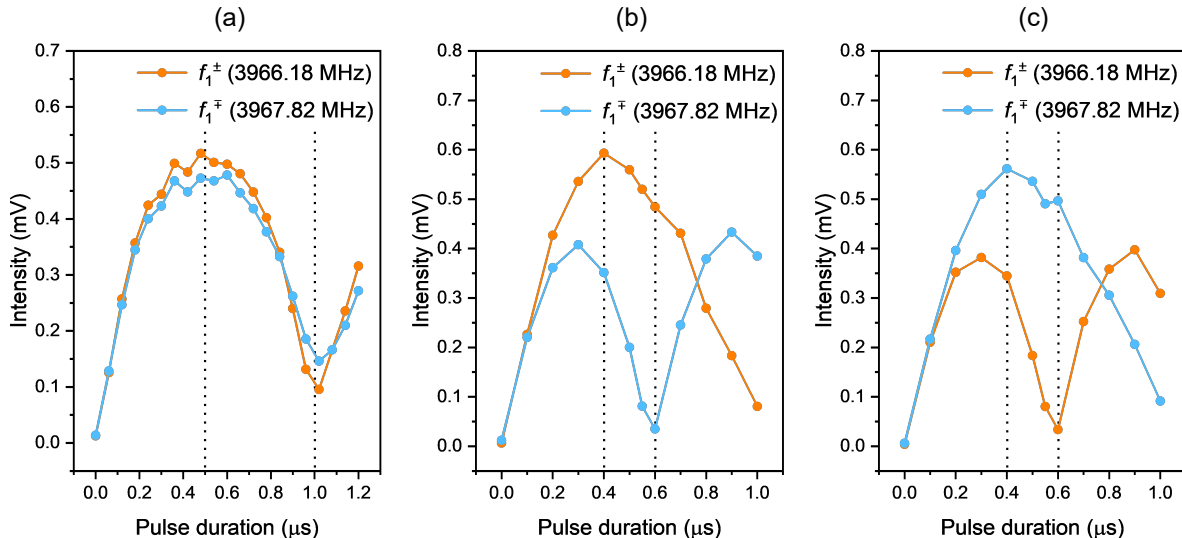


FIG. S8. Nutation curves for the interstate transition #1 in the microwave pulse sequence as a function of pulse duration (μs). The applied excitation frequencies are the center frequency of the tunneling splitting, 3967.0 MHz (a) and the respective splitting components, 3966.18 MHz (b) and 3967.82 MHz (c). The excitation and detection are performed in the same polarization direction. Each point on the curves is from an accumulation of 15000 FIDs.

TABLE S1. Conditions of microwave pulses in the pump-probe scheme, including the associated rotational transitions, frequencies (ν), type of the transitions, power of the microwave amplifiers (P_{amp}), pulse durations at the effective $\pi/2$ ($\tau_{\pi/2}$) and π (τ_{π}) conditions. f_1^c indicates that the frequency of the microwave pulse is at the center of the tunneling components of the f_1 transition, where both components are symmetrically detuned.

Pulse	Transition	ν/MHz	Type	P_{amp}/W	$\tau_{\pi/2}/\mu\text{s}$	$\tau_{\pi}/\mu\text{s}$
f_1^{\pm}	$0_{00}^- - 1_{10}^+$	3966.18	μ_c	50	0.4	1.0
f_1^{\mp}	$0_{00}^+ - 1_{10}^-$	3967.82	μ_c	50	0.4	1.0
f_1^c	$0_{00}^{\pm} - 1_{10}^{\mp}$	3967.00	μ_c	50	0.5	1.0
f_2	$1_{10}^{\pm} - 1_{01}^{\pm}$	1894.35	μ_b	3	0.6	1.6
f_3	$0_{00}^{\pm} - 1_{01}^{\pm}$	2072.65	μ_a	300	0.15	-
f_4	$1_{01}^{\pm} - 2_{02}^{\pm}$	4093.31	μ_a	300	0.2	-
f_5	$2_{02}^{\pm} - 2_{11}^{\pm}$	2293.06	μ_b	3	0.6	1.5

D. Time-resolved pump-probe experiments.

In this section, we discuss the time-resolved pump-probe experiment performed on 3-fluorobenzyl alcohol. The level diagram of the (+)-cycle is shown in FIG. S9, which starts with molecules initially populated in the $|0_{00}^+\rangle$ rotational state. In the pump cycle, two microwave pulses with orthogonal polarizations excite part of the population from the $|0_{00}^+\rangle$ state to the $|1_{01}^-\rangle$ state via a two-photon path: $|0_{00}^+\rangle \xrightarrow{f_1^{\mp}} |1_{10}^-\rangle \xrightarrow{f_2} |1_{01}^-\rangle$. Subsequently, a third pulse in the third mutually orthogonal polarization excites part of the residual population in the $|0_{00}^+\rangle$ state to $|1_{01}^+\rangle$ via a one-photon path: $|0_{00}^+\rangle \xrightarrow{f_3} |1_{01}^+\rangle$. These two excitation paths establish coherence between the $|1_{01}^+\rangle$ and $|1_{01}^-\rangle$ states, for which a direct one-photon transition is dipole-forbidden. This coherence in the $|1_{01}\rangle$ state generates a dynamically localized wavepacket within the double-well system of 3-fluorobenzyl alcohol [1]. Since the two potential wells correspond to the $|R\rangle$ and $|S\rangle$ enantiomeric forms, respectively, the localized wavepacket is chiral and creates an enantiomeric excess that oscillates at the tunneling frequency with a constant amplitude (see Equations 16 and 22). However, this chiral oscillating wavepacket cannot be directly observed, as the $|1_{01}^+\rangle \leftrightarrow |1_{01}^-\rangle$ transition is strictly forbidden, but also as the chiral ensemble does not correspond to any detectable

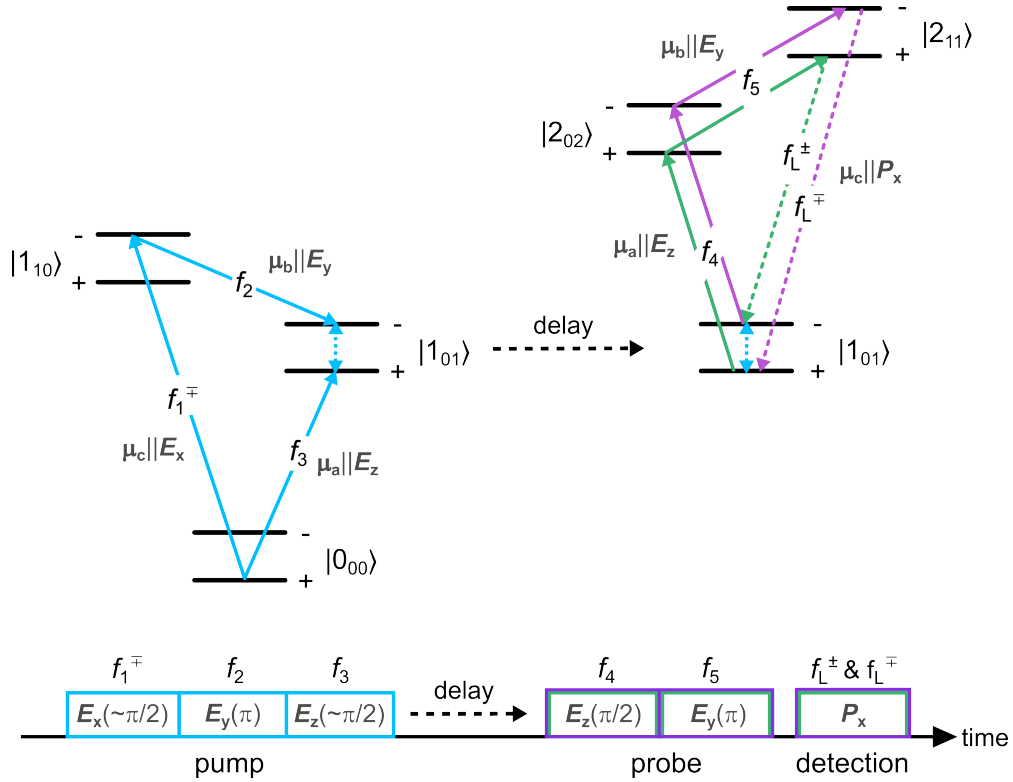


FIG. S9. Pump-probe level diagram starting with the $|0_{00}^+\rangle$ rotational state, hereinafter denoted as (+)-cycle, with the pulse sequence shown below. In the pump cycle, three microwave pulses with mutually orthogonal polarizations induce a coherence between the $|1_{01}^+\rangle$ and $|1_{01}^-\rangle$ states, indicated using a double-headed dotted line. Note that direct excitation of the $|1_{01}^+\rangle - |1_{01}^-\rangle$ transition is dipole-forbidden. This coherent oscillation is subsequently monitored using a probe cycle as a function of time delay. In the probe cycle, the two excitation microwave pulses and the indirectly induced listen signal are also mutually orthogonal to each other. Intrastate transitions are labelled using f_i , while the interstate transition components are labelled explicitly with f_i^\mp/f_i^\pm . For each transition, the corresponding dipole-moment component in the molecular frame and the polarization direction of the microwave field in the laboratory frame are indicated using $\mu_\alpha || \mathbf{E}_\beta$ ($\alpha = a, b, c$; $\beta = x, y, z$). In the pulse sequence, the conditions of the microwave fields are indicated by $\pi/2$ and π , representing the effective $\pi/2$ and π pulse conditions, respectively. The notation $\sim \pi/2$ denotes a condition close to the $\pi/2$ condition. The lengths of the microwave pulses in the sequence are not to scale. (This figure is a copy of FIG. 2a of the main text.)

polarization.

In order to uncover this dynamics, we apply a probe cycle following the pump sequence.

It consists of two excitation microwave pulses (f_4 and f_5) and an emission signal at the listen transitions (f_L^\pm and f_L^\mp). The polarization directions of these three microwave fields are also mutually orthogonal with each other. This configuration enables the simultaneous excitation of two triads in the probe cycle, probing the coherent tunneling dynamics within the $|1_{01}\rangle$ state from opposite directions. One sub-cycle starts from the lower tunneling state $|1_{01}^+\rangle$ and proceeds to the upper substate $|1_{01}^-\rangle$, following the sequence: $|1_{01}^+\rangle \xrightarrow{f_4} |2_{02}^+\rangle \xrightarrow{f_5} |2_{11}^+\rangle \xrightarrow{f_L^\pm} |1_{01}^-\rangle$. The other sub-cycle progresses from $|1_{01}^-\rangle$ toward $|1_{01}^+\rangle$ following the sequence: $|1_{01}^-\rangle \xrightarrow{f_4} |2_{02}^-\rangle \xrightarrow{f_5} |2_{11}^-\rangle \xrightarrow{f_L^\mp} |1_{01}^+\rangle$. As a result, these two probing paths respond oppositely to the chiral coherent oscillation in the $|1_{01}\rangle$ state.

According to the rotational energy diagram of 3-fluorobenzyl alcohol, the tunneling frequency between the $|1_{01}^+\rangle$ and $|1_{01}^-\rangle$ states is about 0.82 MHz. Thereby, measurements with sub- μ s pump-probe delays (t_{pp}) are sufficient to resolve this coherent tunneling oscillation dynamics. As derived in Equations 28–29 (specifically the $\omega_{2t}t_{pp}$ term), the phases of f_L^\pm and f_L^\mp are expected to vary linearly with slopes of $\mp 2\pi \times 0.82$ radians, respectively, as a function of delay time.

The amplitude of the induced listen signal (A_L) relies on the experimental pulse conditions,

$$A_L \propto \sin(\Omega_1\tau_1) \sin\left(\frac{\Omega_2\tau_2}{2}\right) \sin\left(\frac{\Omega_3\tau_3}{2}\right) \sin(\Omega_4\tau_4) \sin\left(\frac{\Omega_5\tau_5}{2}\right) \quad (35)$$

In principle, optimal pulses for f_1^\mp and f_4 should be at the $\pi/2$ condition, while those for f_2 , f_3 , and f_5 should be at the π condition. However, as discussed previously in Section II C, when the f_1^\mp pulse is at its $\pi/2$ condition ($\tau_1 = 0.4 \mu$ s), the f_1^\pm component also gets to a condition near $\pi/2$ (see FIG. S8). The two transitions are not well isolated. Additionally, f_2 and f_3 drive both the $|-\rangle \rightarrow |-\rangle$ and $|+\rangle \rightarrow |+\rangle$ tunneling components of the transitions. This leads to the simultaneous excitation of the (-)-cycle (see FIG. S10) while driving the (+)-cycle, resulting in interference of these two cycles. Both the coherent tunneling dynamics in the $|1_{01}\rangle$ state and the listen transitions (f_L^\pm and f_L^\mp) will be affected by this interference. To reduce the influence of the (-)-cycle, the f_1^\mp pulse is shifted beyond its $\pi/2$ condition to $\tau_1 = 0.6 \mu$ s, where the f_1^\mp transition is at the π condition. In this manner, the strength of the (-)-cycle excitation is reduced to just 1/10 that of the (+)-cycle.

Moreover, a π -pulse of f_3 does not only bring molecules in $|0_{00}^+\rangle$ to the $|1_{01}^+\rangle$ state but also invert the population between the $|1_{01}^-\rangle$ and $|0_{00}^-\rangle$ states. The latter disrupts

the coherence that would otherwise form between the $|1_{01}^- \rangle$ and $|1_{01}^+ \rangle$ states. Thereby, a near $\pi/2$ condition is used for this transition. The experimentally applied pulse conditions

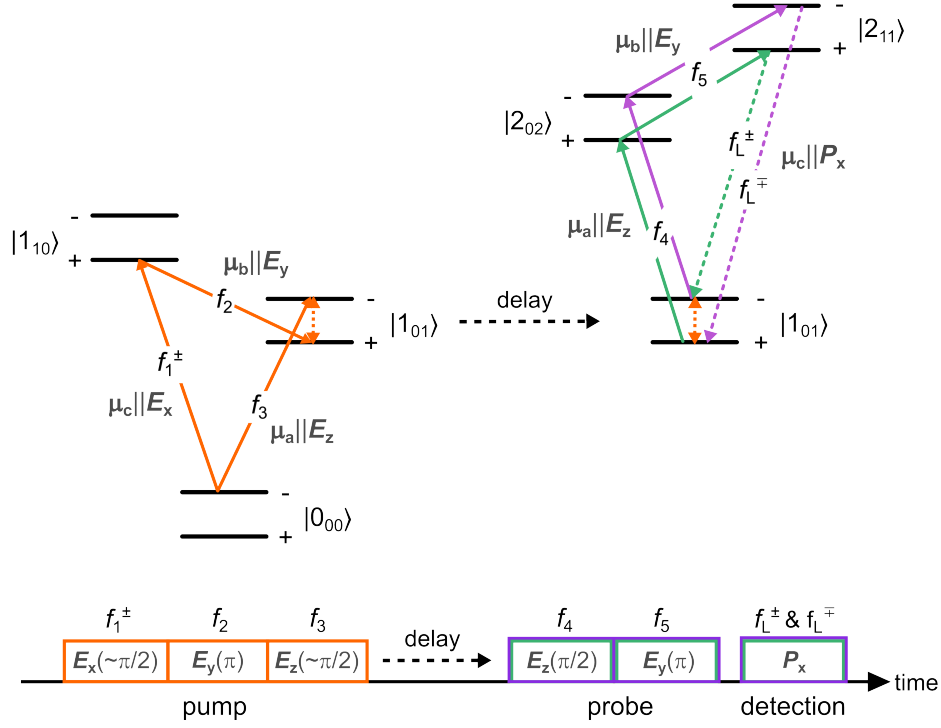


FIG. S10. Pump-probe level diagram starting with the $|0_{00}^- \rangle$ rotational state, hereinafter denoted as (-)-cycle, with the pulse sequence shown below. In the pump cycle, three microwave pulses with mutually orthogonal polarizations induce a coherence between the $|1_{01}^+ \rangle$ and $|1_{01}^- \rangle$ states, indicated using a double-headed dotted line. Note that direct excitation of the $|1_{01}^+ \rangle \rightarrow |1_{01}^- \rangle$ transition is dipole-forbidden. This coherent oscillation is subsequently monitored using a probe cycle as a function of time delay. In the probe cycle, the two excitation microwave pulses and the indirectly induced listen signal are also mutually orthogonal to each other. Intrastate transitions are labelled using f_i , while the interstate transition components are labelled explicitly with f_i^{\mp}/f_i^{\pm} . For each transition, the corresponding dipole-moment component in the molecular frame and the polarization direction of the microwave field in the laboratory frame are indicated using $\mu_{\alpha} || \mathbf{E}_{\beta}$ ($\alpha = a, b, c; \beta = x, y, z$). In the pulse sequence, the conditions of the microwave fields are indicated by $\pi/2$ and π , representing the effective $\pi/2$ and π pulse conditions, respectively. The notation $\sim \pi/2$ denotes a condition close to the $\pi/2$ condition. The lengths of the microwave pulses in the sequence are not to scale.

TABLE S2. Details of the applied microwave pulses in the (+)-cycle for the time-resolved pump-probe experiment, including the rotational transitions, frequencies (ν), type of the transitions, polarizations of the microwave fields in the laboratory frame (\mathbf{E}), power of the microwave amplifiers (P_{amp}), pulse durations (τ_{exp}), and the corresponding Rabi flip angles ($\Omega \cdot \tau$).

Pulse	Transition	ν/MHz	Type	\mathbf{E}	P_{amp}/W	$\tau_{\text{exp}}/\mu\text{s}$	$\Omega \cdot \tau$
f_1^\mp	$0_{00}^+ \rightarrow 1_{10}^-$	3967.82	μ_c	x	50	0.6	$\sim\pi/2$
f_2	$1_{10}^- \rightarrow 1_{01}^-$	1894.35	μ_b	y	3	1.6	π
f_3	$0_{00}^+ \rightarrow 1_{01}^+$	2072.65	μ_a	z	300	0.2	$\sim\pi/2$
f_4	$1_{01}^\pm \rightarrow 2_{02}^\pm$	4093.31	μ_a	z	300	0.2	$\pi/2$
f_5	$2_{02}^\pm \rightarrow 2_{11}^\pm$	2293.06	μ_b	y	3	1.5	π

are summarized in Table S2. Note that the theoretically derived optimal pulse conditions still hold true for f_1 and f_3 if the tunneling transition components can be well isolated by their frequencies, for instance, in the previously investigated system of benzyl alcohol [1]. However, in such systems, owing to the large energy difference (ε_\pm) between the tunneling states, two sets of microwave pulses will be required to drive the two triads in the probe cycle, which is a disadvantage for a proof-of-concept study.

Using the above-mentioned pulse conditions, the five microwave pulses in the (+)-cycle are arranged consecutively in the pulse sequence with a pump-probe delay between the f_3 and f_4 pulses (FIG. S9). Each pulse interacts with molecules in a designated polarization direction by following a specified path in the electronic circuit. The delay time is varied from 0 to 1.3 μs in steps of 0.1 μs , while all other pulse conditions are kept fixed in the experiment. To achieve sufficient signal-to-noise ratios at the listen frequencies (f_L^\pm and f_L^\mp), each point is accumulated from 5×10^5 FID acquisitions, requiring about 2.2 h. As a

TABLE S3. Fitted linear parameters for the phase results of the listen signals, f_L^\pm and f_L^\mp , obtained from the (+)-cycle of the time-resolved pump-probe experiment.

Intercept ($\times 2\pi$, in radians)		Slope ($\times 2\pi$, in radians)		Statistics	
Value	Standard Error	Value	Standard Error	R^2	
f_L^\pm	0.556	0.016	-0.780	0.021	0.991
f_L^\mp	-0.559	0.015	0.873	0.020	0.994

result, the entire scan takes over 30 h. The obtained results have been discussed in detail in the main text, including the evolution of the time-domain frequency beats (FIG. 3 of the main text) and the linear phase-delay dependence of the listen transitions (FIG. 4a of the main text). The parameters obtained from the least-squares fits on the phase results of f_L^\pm and f_L^\mp are provided in Table S3.

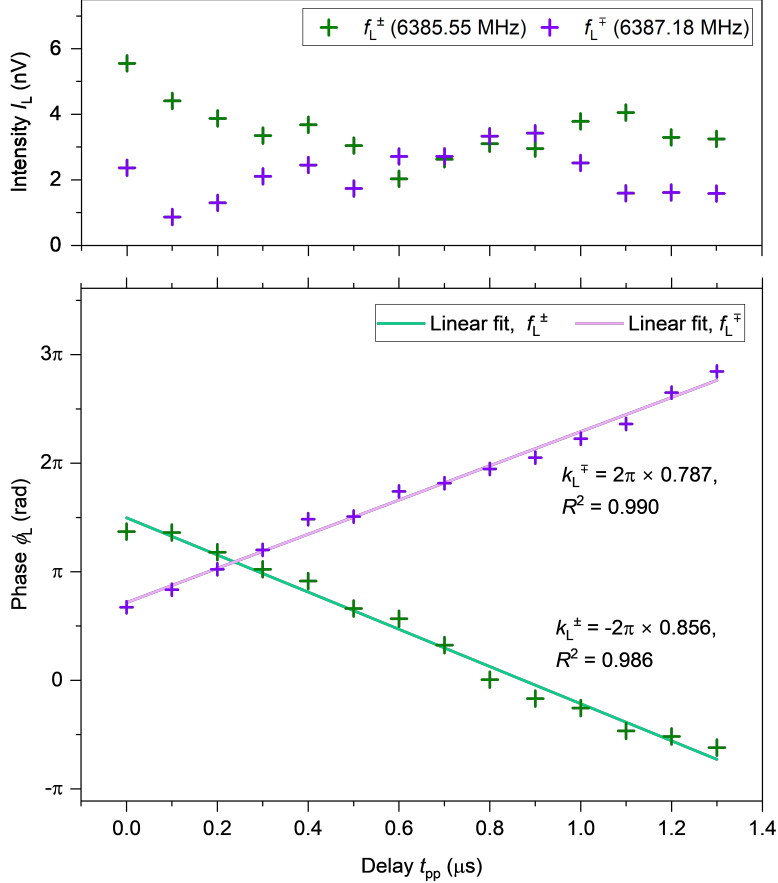


FIG. S11. Results of the (-)-cycle of the time-resolved pump-probe experiment, showing the intensities (A_L) and phases (ϕ_L) at the listen transitions, f_L^\pm (6385.55 MHz) and f_L^\mp (6387.18 MHz), as a function of time delay (t_{pp} , in μs). The scatter points display the experimental results. Each point is averaged from 5×10^5 FID acquisitions, which takes about 2.2 h. The colored lines represent the linear fits of the phase results of f_L^\pm and f_L^\mp , with the slopes (k_L) and R-squared values (R^2) provided.

Similarly, the time-resolved pump-probe experiment is carried out with the (-)-cycle, which begins from the $|0_{00}^- \rangle$ rotational state. The level scheme is given in FIG. S10, and

the pulse conditions are kept identical to the (+)-cycle, except that the f_1^\mp component is replaced with f_1^\pm . The experimental results are presented in FIG. S11, with the linear fitting parameters of the phase results summarized in Table S4. The experimental observations align with the theoretical predictions derived in Equations 30–31, where the phases of f_L^\pm and f_L^\mp in the listen signals exhibit negative and positive linear correlations with the delay time, respectively. Both of the R-squared values (R^2) are close to 0.99. Based on the fitted slopes, the observed tunneling frequencies also deviate from the spectroscopically determined value (0.82 MHz) by approximately 5%, as seen in the experiments with the (+)-cycle [3]. The average tunneling frequency is estimated to be 0.822(19) MHz, highly consistent with the result from the (+)-cycle, which is 0.827(15) MHz.

TABLE S4. Fitted linear parameters for the phase results of the listen signals, f_L^\pm and f_L^\mp , obtained from the (-)-cycle of the time-resolved pump-probe experiment.

	Intercept ($\times 2\pi$, in radians)		Slope ($\times 2\pi$, in radians)		Statistics
	Value	Standard Error	Value	Standard Error	R^2
f_L^\pm	0.749	0.022	-0.856	0.029	0.986
f_L^\mp	0.358	0.018	0.787	0.023	0.990

E. Phase-controlled pump-probe experiments.

As described in Equations 22–23 and 28–31, in addition to the delay modulation, the position of the induced non-stationary wavepacket within the double-well tunneling potential can be precisely tuned by adjusting the phases of the three microwave pulses (φ_1 , φ_2 and φ_3) during the pump excitations. As a result, the phase of the listen signals is linearly dependent on the phases of the pump pulses, while their amplitude remains constant. The phase-phase correlation is expected to be linear (± 1) and to exhibit opposite behaviors for the (+)- and (-)-cycles.

In the phase-controlled pump-probe experiment, we varied the phase of the f_2 pulse (φ_2) in steps of $\pi/6$ radians, with no delay applied between the pump and probe cycles. The obtained listen signals (f_L^\pm and f_L^\mp) from the (+)- and (-)-cycles are depicted in FIG. 4b of the main text and FIG. S12. In both experiments, the signal amplitudes remain relatively constant, showing only regular experimental fluctuations. The signal phases are

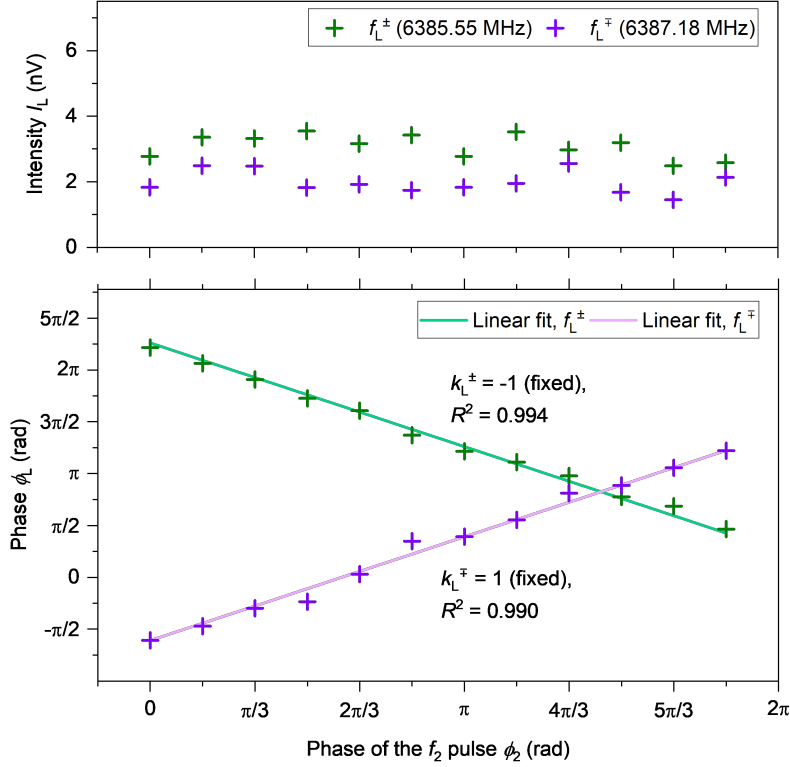


FIG. S12. Results of the (-)-cycle of the phase-controlled pump-probe experiment, showing the intensities (A_L) and phases (ϕ_L) at the listen transitions, f_L^\pm (6385.55 MHz) and f_L^\mp (6387.18 MHz), as a function of the f_2 phase (ϕ_2 , in radians). The scatter points display the experimental results. Each point is averaged from 5×10^5 FID acquisitions, which takes about 2.2 h. The colored lines represent the linear fits to the phase results of f_L^\pm and f_L^\mp , with the slope (k_L) fixed at 1 or -1.

linearly fitted with the slope constrained to 1 or -1, corresponding to the coefficients in the theoretical derivations (Equations 28–31). The R^2 values, close to 0.99, support the expected linear phase dependence.

-
- [1] W. Sun, D. S. Tikhonov, H. Singh, A. L. Steber, C. Pérez, and M. Schnell, Inducing transient enantiomeric excess in a molecular quantum racemic mixture with microwave fields, *Nat. Commun.* **14**, 934 (2023).
- [2] H. J. Metcalf and P. van der Straten, *Laser cooling and trapping* (Springer Science & Business

Media, 1999).

- [3] S. Tang, Z. Xia, A. Maris, and W. Caminati, Tunnelling splittings in the rotational spectrum of 3-fluoro-benzylalcohol, *Chem. Phys. Lett.* **498**, 52 (2010).
- [4] M. Leibscher, E. Pozzoli, C. Pérez, M. Schnell, M. Sigalotti, U. Boscain, and C. P. Koch, Full quantum control of enantiomer-selective state transfer in chiral molecules despite degeneracy, *Comm. Phys.* **5**, 110 (2022).